

Abstract

HOLDER, CHRISTOPHER THOMAS. The Mesoscale Characteristics of Tropical Oceanic Precipitation During Kelvin and Mixed Rossby-Gravity Wave Events. (Under the direction of Sandra E. Yuter.)

We analyze the mesoscale precipitation structures during Kelvin and mixed Rossby-gravity (MRG) wave troughs near Kwajalein Atoll (8.7 °N 167.7 °E) during the 1999-2003 rainy seasons using three-dimensional radar data (radius=157 km) and upper-air sounding data. The large region of anomalously cold cloudiness in the outgoing longwave radiation fields filtered in the wavenumber-frequency domain are suggestive of the presence of the wave trough.

Mesoscale convective systems (MCSs) occur more frequently within Kelvin and MRG wave troughs compared to a multiyear rainy season climatology, but MCS activity widely varies from one trough event to another. Radar volumes during troughs contain only small, isolated rain areas at least half the time, similar to typical Kwajalein conditions and overwhelming many ensemble organizational statistics such as the size, shape, orientation, and reflectivity characteristics of individual contiguous rain areas. This suggests wave trough forcing is variable. Many MCSs contain scattered convective cores and areas of weak reflectivities embedded within the stratiform region, suggestive of perturbations in the MCS air and moisture flow field which may be homogenized away in MCS many schematics and have significant physical implications.

There is an observed limit to convective precipitation area that the atmosphere near Kwajalein can support. This limit is observed in two different datasets near Kwajalein and in the west Pacific warm pool, but the physical reasons for this limit are unclear. Stratiform area fractions vary widely for small total rain areas, and as total precipitation area increases the stratiform area

fraction tends to increase and is less variable. This reflects that small total rain areas contain small rain blobs which often have smaller stratiform proportions than larger blobs.

Kelvin trough mesoscale precipitation structures tend to be slightly more organized than MRG. Total, convective, and stratiform rain areas and MCS rain areas are often somewhat larger during Kelvin troughs, and convective lines occur three to four times more often than during MRG troughs. Enhanced organization of mesoscale precipitation structures during Kelvin events may be linked to stronger, deeper, and more sustained convective updraft regions than MRG troughs, and to a potentially more favorable environment for convective initiation due to enhanced wave dynamics in the convective initiation region than with MRG waves.

The Mesoscale Characteristics of Tropical Oceanic Precipitation During Kelvin and Mixed Rossby-Gravity Wave Events

by

CHRISTOPHER THOMAS HOLDER

A thesis submitted to the Graduate Faculty of

North Carolina State University

in partial fulfillment of the

requirements for the Degree of

Master of Science

MARINE, EARTH, AND ATMOSPHERIC SCIENCES

Raleigh, North Carolina

2007

APPROVED BY:

Sandra Yuter

Chair of Advisory Committee

Anantha Aiyyer

Matthew Parker

Fredrick Semazzi

(i) Acknowledgments

Thanks to George Kiladis of NOAA for providing the OLR dataset and to Peter Blossey of the University of Washington for his blob detection script and assistance with it. Anantha Aiyyer and Adam Sobel were extremely helpful throughout my research in providing detailed technical help and manuscript edits. Thanks also to Casey Burleyson, Catherine Spooner, Kimberly Comstock, Matthew Miller, Steve Nesbitt, and John Russ for their advice and technical help. This study also benefited from discussions with Matthew Parker and Fredrick Semazzi. Thanks also to Sankar Arumugam for substituting for Anantha Aiyyer at my presentation. Thanks also to my parents, and to Brian, who was with me through it all and kept me sane. This study was supported by the North Carolina Space Grant Graduate Fellowship, NASA Grants NN604GA65G and NNX07AD21G, and NSF Grant ATM-0544766.

1. Introduction

Equatorial waves account for a significant percentage of spatiotemporal variance in the satellite-measured outgoing longwave radiation (OLR) spectrum in many tropical locations. The existence, origin, large-scale properties, and convective coupling of various modes of equatorial waves have been extensively investigated since the landmark study by Matsuno (1966), where dry linear shallow water theory was used to derive the equatorial wave dispersion relation. Previous studies have used model reanalysis, satellite observations, or upper-air soundings to detect the fairly regular dynamical and large-scale precipitation patterns associated with the various tropical waves (e.g., Reed and Recker 1971; Hendon and Liebmann 1991; Dunkerton 1993; Dunkerton and Baldwin 1995; Pires et al. 1997).

Many studies have observed the convective coupling of these waves using OLR data (e.g., Hendon and Liebmann 1991; Dunkerton and Baldwin 1995; Magaña and Yanai 1995; Wheeler and Kiladis 1999; Wheeler et al. 2000). Dispersion relations from shallow water theory relate the wavenumber, frequency, equivalent depth, and phase velocity of various equatorial waves, such as Kelvin, equatorial Rossby, mixed Rossby-gravity (MRG), and inertio-gravity (e.g., Matsuno 1966; Lindzen 1967; Lindzen and Matsuno 1968). Some wave characteristics in the real atmosphere diverge from dry theory, which is likely due to convection that couples with the waves and reduces the wave phase speed and equivalent depth below theoretical values (Wheeler et al. 2000). Also, dry theory is linear about a resting state whereas the basic atmospheric state has a complex mean flow. The presence of vertical zonal wind shear mainly tends to couple the barotropic and baroclinic modes of equatorial wave motion (Wang and Xie 1996). The barotropic mode is excited mostly by westward-propagating waves, so zonal vertical shear tends to significantly affect only those equatorial waves that propagate westward.

Under zonal vertical shear, such westward-propagating waves should experience vertical structural asymmetry and slower phase speeds. The structure of eastward-propagating waves should not be significantly affected by shear, and all waves should be at most marginally affected by meridional shear.

Given observed characteristics unique to each wave type, spectral analysis of satellite data isolates global wave activity (e.g., Gruber 1974; Zangvil 1975; Takayabu 1994). Spatiotemporal spectral analysis decomposes time- and space-dependent datasets into frequency-wavenumber components for eastward and westward propagating waves (Hayashi 1982). Wheeler and Kiladis (1999) adapted this analysis with theoretical wave properties and long-term OLR data. Subsequent studies (e.g., Wheeler et al. 2000; Straub and Kiladis 2003a; Straub and Kiladis 2003b; Roundy and Frank 2004) observed large-scale spatiotemporal wave variability and structure and associated convective variability using the Wheeler and Kiladis (1999) methodology. Kelvin and MRG waves have been extensively studied because they are well established in theory and because they explain a significant percentage of tropical OLR variance on the synoptic time scale (Roundy and Frank 2004).

a. Motivation

Previous studies of equatorial waves have dealt with their observed large-scale dynamical structures, their origins, and the large-scale spatiotemporal variance of their associated convection. Only recently have studies begun to apply computationally-intensive global cloud-resolving models to reproduce, on some level, the existence or at least the expected effects of equatorial waves in situations approaching the real atmosphere. These high-resolution modeling studies include those of the UK-Japan Climate Collaboration using the Earth Simulator

(<http://www.earthsimulator.org.uk/>), the Diabatic Acceleration and Rescaling / Reduced Acceleration in the Vertical (DARE/RAVE) methodology (Kuang et al. 2005), and cloud system-resolving models, sometimes used as superparameterizations, within global climate models such as the Community Atmosphere Model (e.g., Grabowski 2003; Randall et al. 2003; Grabowski 2004; Khairoutdinov et al. 2005; Ziemiański et al. 2005). Many models still poorly represent convectively-coupled equatorial waves (e.g., Majda et al. 2004; Yang et al. 2007) and tropical multi-scale interactions in general (Slingo et al. 2007).

We can improve our knowledge and modeling of tropical climatology on large and small scales with better knowledge of the synoptic- and meso-scale structures of waves and associated convection. Houze et al. (2000), for example, used the spatiotemporally dense data network during the Tropical Ocean Global Atmosphere Coupled Ocean Atmosphere Response Experiment (TOGA COARE, Webster and Lukas 1992) to investigate the flow characteristics of super convective systems in two key locations within the Kelvin wave structure – the westerly wind burst area within the large convective region and the westerly onset region closer to the leading edge of the convective region. Houze et al. (2000) found very different momentum feedbacks within these large systems depending on spatial scale and on precipitation dynamics. This highlights the importance of understanding the mesoscale precipitation characteristics of tropical deep convection in order to accurately evaluate scale interactions (Houze et al. 2000).

The goal of this study is to address the largely uninvestigated mesoscale characteristics of precipitation coupled with Kelvin and MRG waves. Kwajalein Atoll (8.7 °N 167.7 °E, Republic of the Marshall Islands) is one of the few open ocean tropical Pacific locations with multi-year datasets of operational weather radar and upper-air soundings that allow us to examine these precipitation structures.

b. Relationship to previous work

This study builds on the work of Swann et al. (2006) (hereafter S06). S06 examined mesoscale precipitation characteristics during significant Kwajalein rain events coincident with significant Kelvin or MRG wave amplitude – that is, significant wave troughs or ridges. In practice, we infer the presents of troughs and ridges of a particular wave type by minima and maxima of OLR after filtering that field to retain only the portion of the spectrum near its theoretical dispersion curve. Throughout this study we use the term ‘wave trough’ to mean the large negative OLR anomalies in the filtered datasets. Likewise, the wave ridge location is suggested by the region of anomalously warm cloud-tops that propagates in tandem with the trough cold cloudiness.

Using contoured frequency-by-altitude diagrams (CFADs, Yuter and Houze 1995), S06 suggested that precipitation areas during Kelvin events may often contain slightly weaker reflectivities than MRG. Weaker total reflectivities imply Kelvin events contain slightly larger stratiform precipitation areas than MRG so long as the Kelvin convective and stratiform reflectivity distributions are similar to those of MRG. Larger stratiform areas suggest enhanced mesoscale precipitation organization during some Kelvin events compared to MRG.

As part of our study, we build on the S06 study by separating their radar reflectivities into convective and stratiform precipitation areas. This allows us to verify that their Kelvin wave events contain larger stratiform precipitation areas than their MRG events. In addition to expanding upon S06, we also repeat and extend their calculations using a different wave event definition that allows us to investigate the mesoscale precipitation structures only within significant wave troughs, excluding those within ridges. We discuss the differences in wave event definitions in more detail in Section a.

Both wave event-defining methodologies have some level of arbitrariness and are arguably valid ways of examining wave-coupled convection. Comparing the results of our methodology with the results of the S06 methodology tests the robustness of these results. Our dataset and the S06 dataset are subsamples of Kwajalein precipitation data, where the S06 dataset represents large rain events and our dataset represents large-scale regimes that we expect to favor convection based on large areas of anomalously cold cloudiness. Considering both the S06 wave events and our wave trough events together, we examine half of the significant rain events in part or in whole that occur during our time period (Section 1). As such, many of the results using both datasets characterize typical Kwajalein precipitation organization. By considering data from both wave types together, we can address not only the differences between wave types, but also the overall characteristics of convection near Kwajalein. For the latter purpose, it would be ideal to examine the entire dataset of three-dimensional radar volumes, rather than just those associated with wave troughs, but this is beyond the scope of this study.

c. Objectives

Our goal is to address the following questions: (1) Which results from S06 are robust to the change in wave event definition? (2) Are there any other significant differences between the mesoscale precipitation structures of Kelvin and MRG waves, besides those found in the brief study of S06? (3) Assuming the samples examined here are representative, what are the general characteristics of mesoscale precipitation structures near Kwajalein? To what extent are these characteristics similar to or different from those found in other studies in other regions?

2. Equatorial Waves

a. Shallow water theory

Matsuno (1966) derived dispersion relations using shallow water theory and an equatorial β -plane. The β -plane approximation allows us to describe the major dynamical equations in Cartesian space rather than in spherical space. With a β -plane, the Coriolis parameter (f) is assumed to vary linearly about a specific latitude through applying a planar surface tangent to that latitude. That is, $f = \beta y$ when the tangential plane is applied at the equator, where β is the Rossby parameter ($\beta = \frac{2\Omega}{a}$, where $\Omega = \text{Earth's rotation rate}$ and $a = \text{Earth's radius}$).

The shallow water theory for equatorial waves begins with the primitive equations of motion, where the Euler equations are simplified by assuming a hydrostatic fluid, using the equatorial β -plane approximation, and neglecting vertical variations. These equations are also linearized about a resting basic state to form what are generally referred to as shallow water equations:

$$\frac{\partial u}{\partial t} - \beta y v + g \frac{\partial h}{\partial x} = 0 \quad (1)$$

$$\frac{\partial v}{\partial t} + \beta y u + g \frac{\partial h}{\partial y} = 0 \quad (2)$$

$$\frac{\partial h}{\partial t} + g \bar{h} \left(\frac{\partial u}{\partial x} + \frac{\partial v}{\partial y} \right) = 0, \quad (3)$$

where t is time, x is east-west distance, y is north-south distance, u is zonal wind velocity, v is meridional wind velocity, g is gravity, and h is perturbation depth whose mean value is \bar{h} (Matsuno 1966). The square of the pure gravity wave velocity (c) can be substituted for ($g\bar{h}$).

Following the assumed exponential wave solution form ($e^{i(kx+\omega t)}$), and after non-dimensionalizing,

Eq. 1-3 can be represented as

$$i\omega u - yv + ik\phi = 0 \quad (4)$$

$$i\omega v + yu + \frac{d\phi}{dy} = 0 \quad (5)$$

$$i\omega\phi + iku + \frac{dv}{dy} = 0 \quad (6)$$

(Matsuno 1966), where ω is frequency, k is zonal wavenumber, and ϕ is geopotential height.

Alternatively, eliminating u and ϕ from Eq. 4-6 results in

$$\frac{d^2v}{dy^2} + v \left(\omega^2 - k^2 + \frac{k}{\omega} - y^2 \right) = 0. \quad (7)$$

Finally, since we consider equatorial wave motions, we apply that $v \rightarrow 0$ when $y \rightarrow \pm\infty$, which requires that $(\omega^2 - k^2 + \frac{k}{\omega} - y^2)$ be an odd integer. Then, 7 can be expressed as

$$\omega^2 - k^2 + \frac{k}{\omega} = 2n + 1 \quad (n = 0, 1, 2\dots) \quad (8)$$

(Matsuno 1966). Odd values of n indicate an equatorially symmetric theoretical dynamic structure, while even values of n indicate equatorial antisymmetry. Negative values of k indicate westward phase speeds and positive values of k indicate eastward phase speeds.

With non-zero n values, each value of n and k has three values of ω that represent westward- and eastward-moving inertio-gravity waves and a westward-moving Rossby wave (Fig. 1). For $n = 0$, only the westward MRG wave and the eastward inertio-gravity wave exist. A unique solution of the primitive equations, with $v = 0$, provides an eastward-moving wave with a phase velocity of a pure gravity wave (Matsuno 1966). In this case, $n = -1$, corresponding to the eastward Kelvin wave (Zangvil and Yanai 1980).

b. Triggering

Two main schools of thought address how equatorial convectively-coupled waves are triggered: deep latent heating and extratropical perturbations. In linear theory, applying a small area of heating to a motionless atmosphere can produce equatorial waves. For example, Gill (1980) used a simple linear model to show that the initiation of an area of heating produces a Kelvin wave that propagates eastward and what he calls a ‘planetary wave’ that propagates westward at about a third of the speed of the Kelvin wave (Fig. 2). Kleeman (1989) used a two-level linear model, with low-level meridional blocking imposed to represent the steep and narrow Andes Mountains, to show that strong diabatic heating from the Amazon forces the transmission of Rossby waves and the reflection of baroclinic Kelvin waves. As might be expected, convectively-coupled wave activity generally has a positive relationship with sea surface temperatures, where warmer waters are preferred locations for deep convection (e.g., Straub and Kiladis 2002; Straub and Kiladis 2003a).

A large portion of equatorial wave events may also be triggered from mid-latitude forcings. Straub and Kiladis (2003a), for example, showed that eastward-moving baroclinic Rossby wave trains in the Southern Hemisphere subtropical jet excite convectively-coupled Kelvin waves. The Rossby wave train provides equatorward transport of wave energy, such as upper-level divergence and vertical motion fields as well as Kelvin wave-like lower-level height and temperature anomalies, that appears to induce OLR anomalies in the Tropics (Fig. 3). These OLR anomalies within the subtropical circulations travel at phase speeds near $15\text{-}20\text{ ms}^{-1}$, which is the typical range of convectively-coupled Kelvin wave phase speeds and is somewhat faster than the subtropical circulation anomalies themselves. Straub and Kiladis (2003a) also observed that latent heating provides the energy to keep Kelvin waves self-sustaining after the wave trains

help them become established.

c. Detection

Since the pioneering shallow water equatorial wave studies of the late 1960s (e.g., Matsuno 1966; Lindzen 1967; Lindzen and Matsuno 1968), many subsequent studies have observed atmospheric perturbations correlating to particular convectively-coupled equatorial waves using sounding data and model reanalyses (e.g., Reed and Recker 1971; Hendon and Liebmann 1991; Dunkerton 1993; Dunkerton and Baldwin 1995; Pires et al. 1997). While the spatiotemporal spectra of tropical clouds are largely red noise, some significant spectral peaks have been observed that seem to correspond to equatorial wave modes (e.g., Gruber 1974; Zangvil 1975; Takayabu 1994). Hayashi (1982) described how space- and time-dependent data can be decomposed with spectral analysis into the component frequencies and zonal wavenumbers for eastward- and westward-moving waves. Wheeler and Kiladis (1999) applied this spectral analysis to satellite OLR data.

The wave-filtering of OLR data is described at length in Wheeler and Kiladis (1999). In that study, OLR data from National Oceanic and Atmospheric Administration polar-orbiting satellites were obtained from 1979 to August 1996. Successively overlapping 96-day time periods by 2 months reduced synoptic and seasonal signals. Because linear theory describes equatorial waves with either equatorially symmetric or equatorially antisymmetric dynamical structures, the gridded OLR data were also decomposed into symmetric and antisymmetric components. Fast Fourier Transforms isolated the frequency-wavenumber spectrum at each latitude, which were then averaged over the time segments of the data period and summed between 15 °N and 15 °S.

They then created a background power spectrum for tropical OLR data by averaging together and smoothing the symmetric and antisymmetric zonal frequency-wavenumber power spectra. Dividing the symmetric and antisymmetric spectra by the background power spectra isolated the basic properties of the various equatorial waves (Fig. 4). These wavenumber, equivalent depth, and periodicity characteristics can then be applied to any particular OLR dataset to isolate the activity of specific equatorial waves and then study their associated large- or small-scale dynamics and precipitation activity.

d. Kelvin waves

The Kelvin wave has a near-equatorial theoretical structure. Figure 5a is the Kelvin wave dynamical structure according to dry, inviscid shallow water theory, with alternating high and low pressures centered on the equator producing equatorially centered areas of convergence and divergence. In filtering long-term OLR data using this assumed equatorially symmetric structure, the global wave-filtered OLR variance associated with Kelvin waves is likewise equatorially symmetric, and Kelvin-band OLR variance is found to maximize between the eastern Indian Ocean and the central Pacific Ocean during Northern Hemisphere summer (Fig. 6a). Despite a general theoretical and observed equatorially symmetric dynamical structure, the maximum OLR signal in the Pacific and Atlantic Oceans is often observed coincident with the warm SSTs of the Northern Hemisphere intertropical convergence zone, or ITCZ (e.g., Straub and Kiladis 2002; Straub and Kiladis 2003a).

A Kelvin wave has an eastward phase speed (individual convergence regions and divergence regions move eastward), an eastward group velocity (envelopes of convergence and divergence move eastward, so that new convective development occurs towards east of current convection),

and westward-moving individual storm cells. The Kelvin eastward phase speed can be seen in Fig. 7a, where individual OLR anomalies move eastward; the eastward movement of groups of positive-negative OLR regions is not always as evident in this figure, which may be due to the chosen OLR shading scale and/or to the reduced spatial plotting resolution resulting from using all longitudes. The convective cloud regions have longitudinal scales on the order of 1000 km (Wheeler et al. 2000) and are often called ‘superclusters’ (Majda et al. 2004). ‘Westerly wind bursts’ are often associated with Kelvin waves, especially in the west Pacific warm pool region (e.g., Kiladis et al. 1994; Lin and Johnson 1996; Johnson and Lin 1997; Houze et al. 2000). Among the frequencies retained after filtering to remove some diurnal and seasonal signals, Kelvin waves are associated with at least 20% of the local OLR variance near the equator and along the North Pacific ITCZ during Northern Hemisphere spring and summer (Roundy and Frank 2004).

Kelvin waves exist over a wide range of zonal wavenumbers, wave periods, and equivalent depths, and the preferred values of these characteristics can also vary with location. Fig. 4b indicates expected Kelvin wavenumbers from +1 to +14, periods from near 30 days to near 2.5 days, and equivalent depths from 8 m to 90 m. The typical Kelvin wave phase speed in the Pacific region, corrected for background flow, is near 17 ms^{-1} (Wheeler and Kiladis 1999), so the observed uncorrected velocity of Kelvin convective regions is typically closer to 10 ms^{-1} because it moves against the background easterly trade winds.

e. MRG waves

The MRG wave has a theoretical equatorially antisymmetric dynamical structure (e.g., Zangvil and Yanai 1980; Zangvil and Yanai 1981; Hendon and Liebmann 1991; Dunkerton

1993; Dunkerton and Baldwin 1995; Wheeler and Kiladis 1999). Figure 5b shows the theoretical MRG dynamical structure, with alternating high and low pressures to the north of the equator and opposing pressure centers to the south of the equator. This pressure setup likewise produces alternating equatorially antisymmetric areas of convergence and divergence. When OLR data are filtered for MRG waves assuming equatorial antisymmetry, the OLR variance associated with MRG waves is antisymmetric and maximizes near the dateline in the central Pacific during Northern Hemisphere autumn (Fig. 6b, Wheeler and Kiladis 1999). This maximum variance location is near our study region of Kwajalein.

A MRG wave has a westward phase speed (individual convergence and divergence regions move westward), an eastward group velocity (envelopes of ascent and descent move eastward, so that new convective development occurs east of current convection), and westward-moving individual convective elements. Figure 7b shows this, where OLR anomaly envelopes move eastward but individual anomalies move westward. Of the frequencies retained after filtering out some diurnal and seasonal signals, MRG waves are associated with about 5% of the global convective variance in OLR with a broad maximum near the end of Northern Hemisphere summer (Roundy and Frank 2004). Visually examining the variance near Kwajalein of the other wave-filtered OLR signals (Wheeler et al. 2000 Fig. 3, parts (a) and (e) are reproduced in our Fig. 6 for Kelvin and MRG, respectively), MRG-related OLR variance is much less than that of Kelvin waves, slightly less than that of equatorial Rossby waves, similar to that of eastward inertio-gravity waves, and much greater than that of $n=1$ and $n=2$ westward inertio-gravity waves.

MRG waves exist over a range of zonal wavenumbers, wave periods, and equivalent depths that is smaller than with Kelvin waves. Figure 4a indicates expected MRG wavenumbers from

-1 to -10, periods from near 9 days to near 3 days, and equivalent depths from 8 m to 90 m. The typical MRG wave phase speed in the Pacific region is near 5 ms^{-1} after correction for the background flow speed (Wheeler and Kiladis 1999), though since MRG waves travel with the background easterly trade winds, the observed speed of MRG-associated convective regions can be near $25\text{-}30 \text{ ms}^{-1}$.

3. Data and methodology

a. Identifying Kelvin and MRG waves

Kelvin and MRG waves are identified for 1997-2005 with the OLR frequency-wavenumber spectral analysis method described in Wheeler and Kiladis (1999). Wave-filtered OLR data are calculated using twice-daily (06 UTC and 18 UTC) NOAA polar orbiting satellite data interpolated in space and time as in Liebmann and Smith (1996). We require that the filtered anomalies retain the equatorial symmetry properties described in theory on a resting basic state: the Kelvin OLR structure is equatorially symmetric, MRG is antisymmetric. When we remove these symmetry constraints, as some previous studies have done (e.g., Straub and Kiladis 2002; Straub and Kiladis 2003a; Straub and Kiladis 2003b; Roundy and Frank 2004), we generally arrive at the same trough events as when using symmetry, with some small differences in event duration.

As indicated in Figure 4, Kelvin waves are filtered using equivalent depths of 8 to 90 m, zonal wavenumbers of +1 to +14, and frequencies of 0.03 to $0.4 \text{ cycles day}^{-1}$ (wavelengths 33.3 days to 2.5 days). MRG waves are filtered using equivalent depths of 8 to 90 m, zonal wavenumbers -1 to -10, and frequencies of 0.12 to $0.34 \text{ cycles day}^{-1}$ (wavelengths 8.3 days to

2.9 days). These equivalent depths are calculated based on the zonal wavenumbers, meridional wavenumbers, and frequencies coincident with the wave-filtered OLR spectral peaks in Figure 4.

Details of our trough event-defining methodology and the wave event-defining methodology of S06 are highlighted in Table 1. The wave-filtered OLR anomaly fields for each satellite scan are spatially averaged across a $7.5 \times 7.5^\circ$ box centered over Kwajalein – 5 to 12.5° N, 162.5 to 170° E. This provides a single average OLR anomaly at each time for the Kwajalein region. We then look for strong negative wave-filtered OLR anomaly values in our time period (the rainy seasons, or July-December, of 1999-2003) by comparing these OLR anomalies to the mean and standard deviation OLR anomalies using a longer time span – the rainy seasons of 1997-2005. Specifically, during the rainy seasons of 1999-2003, wave trough events are defined as periods of at least 24 h (3 satellite scans) where the negative wave-filtered OLR anomaly amplitudes are at least 1.5 standard deviations (σ) larger than the mean anomaly amplitudes of the 1997-2005 dataset. For Kelvin OLR anomalies, $\sigma = 7.1244 \text{ Wm}^{-2}$ about a mean of -0.0082 Wm^{-2} , while for MRG $\sigma = 4.7890 \text{ Wm}^{-2}$ about a mean of -0.0028 Wm^{-2} . During our 30 month study period, this methodology identifies 23 Kelvin troughs events, corresponding to 25.5 Kelvin event-days, and 16 MRG trough events, corresponding to 16 MRG event-days. For $\sigma=2$, too few trough events are identified for our results to be robust, while $\sigma=1$ results in many weaker trough events.

The composite wave-filtered and raw OLR anomalies for the trough events are shown in Figure 8 for Day -2, Day 0, and Day +2. Strong Kelvin and MRG negative wave-filtered OLR anomalies pass near Kwajalein at Day 0. This is also visible in the composite raw OLR data. Despite the large frequency filtering window for Kelvin waves, the composite period

of our chosen Kelvin wave trough events is five days. This is evident by the amount of time between one wave trough passing Kwajalein and the next wave trough. Based on Figure 4, this periodicity indicates a zonal wavenumber between +3 and +11 and a composite phase speed, based on distance covered by the trough per unit time, near 13 ms^{-1} without correction for the background flow. The composite MRG period is also five days, suggesting a zonal wavenumber between -1 and -7 and an uncorrected composite phase speed near 32 ms^{-1} .

S06 examined a smaller sample of times than in our study (Table 1). S06 used radar data from July-December 1999-2001 and July-September 2002 to identify times with rain areas exceeding the Kwajalein mean rain area by 2σ – a ‘rain event-centric’ approach. They identified Kelvin and MRG wave activity, coincident with those rain events, whose squared OLR anomaly amplitude exceeded 2σ across the spatial domain 0 to 15°N , 165 to 170°E . With this definition, S06 identified 22 Kelvin wave events and 22 MRG wave events, corresponding to 52 Kelvin event-days and 48 MRG event-days. In S06, examining both wave ridges and troughs allowed for the possibility of wave-related convection lagging or leading the trough due to the dynamics of individual storms.

Our methodology focuses specifically on the mesoscale precipitation structures within equatorial wave troughs. In not requiring a rain area threshold, our wave event definition is ‘wave event-centric’. Only 15 of 75 S06 Kelvin wave event-days and 5 of 48 S06 MRG wave event-days correspond to our Kelvin and MRG trough event days.

b. Radar data

1) KWAJALEIN RADAR

Table 1 of Houze et al. (2004) provides the characteristics of the Kwajalein operational S-band radar. Three-dimensional radar volumes, completed in 10-12 min intervals, are quality controlled as described in Sobel et al. (2004). Meteorological echoes within $17 \text{ km} \leq \text{radius} \leq 157 \text{ km}$ are interpolated to a Cartesian grid with 2 km horizontal and vertical grid spacing. Radar calibration corrections (Table 2) follow Houze et al. (2004). Periods without a specified correction (48% of our data) are not calibrated (Table 3). In all, 3609 radar volumes were available for our Kelvin trough times and 2028 for MRG troughs.

A single-elevation long-range (radius=240 km) scan follows each volume scan. The entire rainy season 1999-2003 time series of long-range scans had been processed for the Kwajalein Storm Finder web page (<http://www.atmos.washington.edu/~dpodhola/kasf/>). In the case of three-dimensional radar volumes, only those specific to the wave event time periods of S06 and this study are processed. We use the complete long-range scan dataset to describe ‘typical’ Kwajalein rain areas. Early July 1999 and nearly all of October-December 2002 are missing from the long-range dataset due to radar malfunctions. These periods contain three Kelvin trough events (events 1, 15, and 16, Fig. 5) and one MRG trough event (event 15). Two of these trough events produced very large rain areas within the three-dimensional radar volume dataset; the two other events contained relatively small rain areas.

Long-range scan rain areas during the available Kelvin and MRG trough events were often larger than typical Kwajalein rain areas (Table 4). Our trough events account for 5% of the long-range radar scans but 7% of the rain area during the 1999-2003 rainy seasons. Consid-

ering rain area as a proxy for rain rate (Section 4), the mean area-averaged rain rate during trough events is 1.3 times greater than that of the long-term dataset. As such, Kelvin and MRG troughs are generally preferred locations for MCSs compared to longer-term precipitation data at Kwajalein. The S06 dataset accounts for 17% of scans but 27% of rain areas in the long-term dataset, with a mean area-averaged rain rate during wave events that is 1.6 times greater than that of the long-term dataset. Our trough dataset and the S06 wave dataset together account for 20% of long-range radar scans and 30% of long-range rain areas, with a mean area-averaged rain rate that is 1.5 times greater than that of the long-term dataset. Larger trough rain areas are consistent with Reed and Recker (1971), who investigated 18 tropical synoptic waves just west of the Marshall Islands and found higher rainfall accumulations in wave troughs.

We detail below the various methods we use to describe precipitation organization using radar data. Visual examination of horizontal radar reflectivity data is a basic and subjective analysis (Section 3 below), while ‘blob’ identification is a more objective identification of the two-dimensional characteristics of individual contiguous precipitation regions (Sections 4 and 5). Separating precipitation areas into convective and stratiform precipitation allows us to analyze the general dynamical nature of precipitation (Section 2), while CFADs indicate vertical reflectivity distributions and precipitation echo heights (Section 6).

2) CONVECTIVE AND STRATIFORM SEPARATION

Separating radar reflectivity into the dynamically distinct convective and stratiform precipitation structures sheds further light on the intensity and mesoscale organization of rainfall (Houze 1997). Viewing precipitation areas categorized in this manner also aids in the visual interpretation of precipitation organization (e.g., Rickenbach and Rutledge 1998). Convective

and stratiform precipitation maps are derived from interpolated reflectivity fields for the 0-2 km altitude layer of each radar volume following the separation methodology described in the ‘This Study: best’ category of Table B1 in Yuter et al. (2005). This separation is based on the algorithm developed by Steiner et al. (1995) for 2x2 km radar data near Darwin, Australia. Yuter et al. (2005) tuned the algorithm for hardware and conditions specific to Kwajalein. In this algorithm, convective cores are identified by pixels whose near-surface reflectivity is greater than 40 dBZ or by pixels satisfying:

$$\Delta Z_{cc} \geq 8 \cos \left(\frac{\pi Z_{bg}}{110} \right),$$

where ΔZ_{cc} is the difference between the reflectivity of one pixel and the average reflectivity of raining pixels within 11 km radius of that one pixel (Z_{bg}). Values of ΔZ_{cc} range from 8 dB for ($Z_{bg} \sim 0$ dBZ) to 1 dB for ($Z_{bg} \sim 50$ dBZ).

The convective region about the convective core, or ‘convective radius’ (R), is based on Z_{bg} and ranges from 1 km for convective pixels of lesser reflectivity to 5 km for convective pixels of greater reflectivity:

$$\begin{aligned} R &= 1 && \text{for } Z_{bg} < 15 \text{ dBZ} \\ R &= 2 + \frac{Z_{bg} - 15}{5} && \text{for } 15 \text{ dBZ} \leq Z_{bg} < 30 \text{ dBZ} \\ R &= 5 && \text{for } Z_{bg} \geq 30 \text{ dBZ}. \end{aligned}$$

All other near-surface pixels > 15 dBZ, corresponding to rainrates $> 0.32 \text{ mmhr}^{-1}$ (Houze et al. 2004), are considered stratiform, and those ≤ 15 dBZ are denoted ‘weak’. It is possible for

convective cores to have reflectivities ≤ 15 dBZ if they have significant reflectivity gradients with surrounding pixels, but this only occurs for 0.3% of trough convective cores. When precipitating areas are examined in Sections 4 and 6, only convective and stratiform reflectivities are considered to be raining at the surface, and weak reflectivities are excluded. The ‘total precipitation area’ in a given radar scan is the sum of convective and stratiform precipitation areas in that scan. Likewise, ‘convective precipitation area’ and ‘stratiform precipitation area’ refer to the scan-wide convective and stratiform areas. Figure 9 provides two examples of radar reflectivity scans (a,d) and their corresponding convective-stratiform-weak maps (b,e).

3) VISUAL ORGANIZATION CLASSIFICATION

We visually examine convective-stratiform-weak maps at 30 min intervals for all the Kelvin and MRG radar volumes in our trough dataset (e.g., Fig. 9b,e). Organizational categories are: convective lines (with subsets based on associated stratiform regions), medium-sized non-MCS stratiform areas with embedded convection, MCSs, and isolated. These categories are mutually exclusive. Multiple types of organization can coexist.

Convective lines are at least 100 km long (e.g., Parker and Johnson 2000) and must exist for at least 30 min within the radar domain (radius=157 km). Lines can have leading-, trailing-, or parallel-stratiform structures (e.g., Parker and Johnson 2000), where we require the stratiform region to be at least 50 km wide along at least half the line. Any other convective line is called ‘line’.

‘Medium-sized’ blobs have rain areas of at least 2500 km² with at least three embedded convective cores but do not attain MCS status. MCSs are blobs with rain areas of at least 2500 km² and length scales that are at least 100 km (Houze 2004) and are no more than twice the

width scale (Section 4 explains measuring blob axes). Fourteen of 30 identified convective lines could also be classified as MCSs based on these criteria. We do not note these convective lines as MCSs in our organizational statistics, which reduces the percentage of 30-min radar volumes containing MCS from 19% to 18%.

Blobs not fitting the above categories are 'isolated'. If less than 10 isolated blobs totaling less than 900 km² rain area coexist with another organization, we do not note isolated activity.

These various time and space requirements are somewhat arbitrary, but they are relatively easy to visually measure and provide a clearly defined rubric for horizontal organization classification. Only 3% of the half-hour Kelvin scans and 2% of half-hour MRG scans are missing or showed no activity. The organizational statistics in Section 5 are for these active half-hour radar scans unless otherwise noted.

4) CONTIGUOUS RAIN AREA 'BLOB' ANALYSIS

We use a 'blob analysis' algorithm (Peter Blossey of the University of Washington, see <http://www.atmos.washington.edu/~bloss/blobcount/> for algorithm details) to objectively analyze individual contiguous rain area 'blobs' in the 0-2 km altitude layer of each radar reflectivity volume. This algorithm is similar to the precipitation feature methodology in Nesbitt et al. (2000). Pixels with reflectivities exceeding 15 dBZ must share at least one full side to be contiguous. The algorithm can determine the number of blobs; the number of contiguous reflectivity pixels per blob (blob rain area); the distance between blob centroids; and blob reflectivity statistics. Figure 9 shows two examples of radar reflectivity (a,d) scans and their corresponding blob analysis maps (c,f).

Blob shape and azimuthal orientation are determined using the second moment of inertia

tensor eigenvalues of each blob (Medioni et al. 2000), which provide ellipse-fitting major and minor axes lengths. This ellipse-fitting technique has been used with satellite radar data in the tropics and subtropics (e.g., Nesbitt et al. 2006, their Fig. 1d reproduced as our Fig. 10). The length ratio of minor-to-major axes is the blob’s ‘aspect ratio’, and the blob azimuthal orientation is the angle of the major axis clockwise from north. Blobs with less than 10 pixels ($< 40 \text{ km}^2$) are too small to determine orientation or aspect ratio, so we analyze these two characteristics only for the 46% of blobs containing at least 10 pixels.

We apply a 15 dBZ reflectivity detection threshold. In varying the threshold from 0 dBZ to 25 dBZ, the cumulative number of detected blobs across the ensemble of trough radar volumes is fairly constant. Other characteristics (e.g., aspect ratio, orientation, and reflectivity modes and maxima) are insensitive to altering reflectivity thresholds below about 25 dBZ.

Quality control processing of the radar data removes clutter-prone reflectivity data within 17 km of the radar and creates a ‘center hole’ of area $A_c = 708 \text{ km}^2$ in each radar scan (e.g., Figs. 9b,d,e). About 10% of our blobs occupied the ‘center hole’, so that the blob algorithm could not calculate their full areas. The area of each of these blobs is augmented by $\frac{i}{44} \cdot A_c$, where i is the number of the ‘perimeter pixels’ (44 total) that the blob contains. This changes only the calculated size of the blob.

5) POROSITY WITHIN CONTIGUOUS RAIN AREA ‘BLOBS’

Many MCSs contain holes in their precipitation field where reflectivities are weak or nonexistent (e.g., the dark blob in Fig. 9f, with interior holes indicated as white space). We define an MCS with these reflectivity holes to be ‘porous’. Porosities imply perturbations in the moisture and flow fields that are represented as continuous within MCS schematics that are based on

averaged MCS structure. Upon browsing aircraft radar data from TOGA COARE (Yuter et al. 1995), we found that MCSs in the west Pacific warm pool region are also frequently porous. We quantify MCS porosity near Kwajalein in our trough dataset.

Porosity is defined as areas with reflectivities less than or equal to 15 dBZ surrounded by areas with reflectivities exceeding 15 dBZ. To quantify MCS porosity, (1) we identify the perimeter pixels of each MCS across all trough radar volumes (e.g., ‘chain code’, Russ 1995). Then, (2) the area (A) inside the perimeter is calculated as $A = \frac{1}{2} \sum_{k=1:n-1} [(X_k \cdot Y_{k+1}) - (X_{k+1} \cdot Y_k)]$ (Russ 1995), where X and Y are of length n and contain the x and y coordinates of the perimeter pixels, with the first pixel coordinates repeated at the end. Finally, (3) given MCS rain area (S) without correction for the ‘center hole’ underestimation discussed in Section 4, we calculate MCS porosity $P = 1 - (\frac{S}{A})$.

Pixel coordinates are defined as the center of the pixel, so part of each perimeter pixel is excluded in the area calculation. Two methods for improving the A estimation are tested on shapes of known area: (i) subdivide radar pixels to reduce how much of each perimeter pixel is excluded from A ; (ii) assume that an average of half of each perimeter pixel is excluded from A and add this estimated missing area to A . The most computationally efficient method that provided the correct answer was halving the grid spacing, performing steps (1) and (2), and implementing step (ii). That is, the 2x2 km radar pixels are each subdivided into four 1x1 km pixels, steps (1) and (2) are performed, the area of half of each perimeter pixel (0.5 km^2) is added to A , and step (3) calculates porosity.

Blob porosity does not depend heavily upon the blob detection reflectivity threshold. Many of the porosity holes will shrink somewhat at lower reflectivity thresholds, depending on the horizontal gradient of reflectivity surrounding the hole. However, lowering the reflectivity thresh-

old also tends to increase the horizontal expanse of blobs, which can lead to new reflectivity holes in areas that are not encompassed by the blob at a 15 dBZ threshold. Thus, the porosity statistics change only slightly if the reflectivity threshold is reduced to, for example, 5 dBZ.

6) CFADS AND EFFECTIVE ECHO HEIGHTS

CFADs of the Kelvin and MRG convective and stratiform reflectivity volumes are created to examine joint frequency distribution of reflectivities with height across the ensembles of Kelvin and MRG data. To construct a CFAD, a histogram of reflectivity frequency is calculated for each altitude layer of the radar volume and normalized by the number of data points in that level. These histograms are then contoured. A CFAD summarizes the vertical reflectivity characteristics of the ensemble of rain areas. We compose CFADs for reflectivities from -15 to 60 dBZ, every 1 dB, with contour intervals of $0.125\% \text{ data dBZ}^{-1}\text{km}^{-1}$.

The frequencies of rain echo heights are also calculated using CFADs. Absolute echo top height (the highest height containing any reflectivity) is generally a poor indicator of the internal dynamical structure of convection (DeMott and Rutledge 1998). To be more representative of the convective structure, we calculate each volume's 75th percentile echo area height. The precipitation area in each altitude layer of the radar volume is summed into a volume-total precipitation area. Then, for each radar scan, we note the lowest altitude layer below which exists at least 75% of the volume-total precipitation area. This effective echo height calculation is similar to that used in Yuter (2004).

c. Atmospheric sounding data

Twice-daily Kwajalein upper-air soundings for the 1999-2003 rainy seasons are obtained from the National Climatic Data Center Integrated Global Radiosonde Archive (<http://www.ncdc.noaa.gov/oa/climate/igra/index.php>). Data at the mandatory levels are interpolated to finer vertical resolution as in Sobel et al. (2004) – every 10 hPa from 1000-860 hPa, every 25 hPa from 850-25 hPa. No temporal interpolation was applied. Zonal and meridional winds and specific humidity are calculated. Sounding anomalies are calculated by removing the five-day 1976-2005 mean values from each sounding day. For example, for the 12 UTC 15 August 2001 sounding, the ten 13-17 August soundings for each year 1976-2005 are averaged into one sounding and subtracted from the 12 UTC 15 August 2001 sounding to create the 12 UTC 15 August 2001 sounding anomaly.

It is difficult to quantitatively compare our time lag composites of vertical temperature, winds, and moisture to other studies that used larger datasets (e.g., Wheeler et al. 2000; Straub and Kiladis 2002; Straub and Kiladis 2003b; Majda et al. 2004) because of our relatively small sample size of soundings – 59 Kelvin soundings, 33 MRG soundings. Instead, we qualitatively evaluate these variable composites. Figure 11a,c,e shows the Kelvin and MRG sounding composites before and after the passage of the wave trough at Day 0, and Figure 11b,d,f shows similar plots for a single Kelvin wave during the Tropical Eastern Pacific Processes Study (TEPPS, Yuter and Houze 2000 and Yuter et al. 2000; these figures correspond to Figures 10, 14, and 11, respectively, of Straub and Kiladis 2002). These lag composites can also be thought of as spatial composites, where Kelvin waves move west to east (left to right) and MRG waves, with the time axis reversed, move east to west (right to left). The lengths of the composite Kelvin and MRG time axes are each five days and represent one ridge-trough-ridge wavelength. Any

regions in the wave sounding composite significantly different from the larger dataset of all 1999-2003 soundings (to 90% using a Student's t-test) are outlined in bold contour.

Vertical temperature anomalies have been widely documented to vertically alternate between warm and cool through the depth of the troposphere during wave events (e.g., Fig. 11b for Kelvin, from Straub and Kiladis 2002). Vertical temperature composites for our dataset (Fig. 11a) show significant warm anomalies and near-zero anomalies alternating with height. Both wave types display a large moist anomaly through low- to mid-levels (Fig. 11c), though they do not clearly show any tilt with height as may be expected (e.g., Fig. 11d for Kelvin, from Straub and Kiladis 2002). Previous studies have observed a 'boomerang' shaped negative zonal wind anomaly within Kelvin and MRG wave troughs, where the boomerang vertex is often near 100 hPa (e.g., Fig. 11f for Kelvin, from Straub and Kiladis 2002). The Kwajalein sounding data are generally sparse and unreliable beyond 100 hPa, but there is some indication below 100 hPa of the first half of the negative zonal wind anomaly boomerang (Fig. 11e). These sounding composites, in addition to the wave-filtered and raw OLR anomalies and ensemble rain areas (Fig. 8, Section a), help ensure that we are identifying significant Kelvin and MRG trough activity near Kwajalein.

d. Significance

We perform some calculations of statistical significance in this study. One is the Student's t-test, which we perform on sounding data (Section c) to compare observations during Kelvin and MRG waves to the background climatology. The other is a 10 000-member Monte Carlo test, which is used to compare rain area frequency distributions between the Kelvin and MRG datasets. In the Monte Carlo test, we combine the 3609 Kelvin and 2028 MRG radar volumes

into a superset and use a random number generator to randomly assign 3609 volumes as Kelvin and 2028 volumes as MRG. This is performed 10 000 times. Rain area statistics are calculated for each iteration. We compare the magnitude of the difference between the two randomly generated frequency distributions for each area bin to that of the original frequency distribution. For the magnitude difference between the MRG and Kelvin distributions in a particular area bin to be considered significant to 95%, at least 9500 of the random iterations must produce smaller differences in that bin.

Note that mathematical significance may not always have a clear physical explanation. Though most of the differences in precipitation organization between Kelvin and MRG were small, some were statistically significant. Some of these differences imply that Kelvin troughs mesoscale precipitation structures may more often be more organized than those of MRG troughs, while the physicalities of other significant differences are unclear.

e. Definition of organization

With only one weather radar and a single site that launches upper-air soundings only twice daily, our meteorological observations at Kwajalein lack the spatiotemporal resolution to thoroughly explore mesoscale precipitation dynamics such as cold pools, vertical motion, and divergence profiles. Outside of a field project, studies over the open ocean must rely on reanalyses for detailed dynamical studies. Reanalyses can often be unreliable across the oceanic tropics because of sparse observed data.

Utilizing reanalyses is beyond the scope of our observational study. Instead, we infer general, relative mesoscale precipitation organization based on comparatively larger rain areas, which must contain persistent mesoscale circulations to reach and sustain such areas, and on

the general appearance of MCSs and convective lines. Larger rain areas should contain more persistent mesoscale circulations that enhance precipitation vigor beyond what is observed in smaller areas (Yuter 2004), likely enhancing the ability of the environment to support and sustain greater areas of convective precipitation and support a more efficient and sustained ‘conversion’ of convective precipitation into more widespread stratiform precipitation (Houze 1997; Yuter and Houze 1998). Such mesoscale circulations should increase the efficiency and amount of hydrometeor growth through stronger or more sustained convective updrafts and longer time periods within the stratiform region for growth through vapor deposition and aggregation. These circulations should also increase the horizontal expanse of the storm through longer and more continuous cross-storm flows.

Our organizational statistics should not be sensitive to sea surface temperature (SST) because the peaks in rainy season SST varied by only about 0.5 °C in our dataset. There also appears to be no strong correlation between the phase of the El Niño-Southern Oscillation and wave activity or wave event rain areas.

4. Total precipitation area

The total areas of precipitation in the 0-2 km altitude layer for both Kelvin- and MRG-related events had frequency distributions that were skewed lognormal (Fig. 12, Table 7). This distribution indicates that total rain areas were usually small. We found a similar distribution when we used the S06 dataset.

Lognormal frequency distributions are common with cloud and radar horizontal size distributions across the tropics (López 1977). These distributions of total precipitation areas, and

of individual contiguous precipitation areas (see Section 5, Fig. 15), during our trough events are consistent with previous studies at Kwajalein and elsewhere in the tropics (e.g., Houze and Cheng 1977; Yuter et al. 2005; Cetrone and Houze 2006). This rain area distribution was also seen in a 1999-2001 Kwajalein radar climatology performed by Yuter et al. (2005), and Cetrone and Houze (2006) observed a lognormal rain area frequency distribution in their samples from the Kwajalein Experiment (KWAJEX, e.g., Yuter et al. 2005).

Kelvin trough events contained significantly greater frequencies of total precipitation areas covering more than about 40% of the radar domain ($\geq 30\,700\text{ km}^2$). Three Kelvin trough events produced rain areas that were larger than those of any MRG event, and eight Kelvin events reached larger rain areas than were observed in all but two MRG events. While we sample more Kelvin events than MRG (23 vs. 16), this difference is larger than one would expect due purely to sampling error. Larger rain areas should contain more persistent mesoscale circulations than smaller areas, so the large total precipitation areas associated with some Kelvin events suggest that the mesoscale kinematic structures associated with Kelvin troughs were frequently slightly more organized than during MRG troughs.

5. Visual Organization

a. Isolated Activity

As suggested by the skewed lognormal distributions of total precipitation area, the troughs of both wave types very frequently contained small, isolated convective activity (e.g., Fig. 9a-c). Of the half-hour scans containing precipitation, 95% of Kelvin scans and 93% of MRG scans had isolated precipitation areas, and 56% and 50% of Kelvin and MRG scans contained only

isolated activity (Fig. 13, Table 5). Very frequent small, isolated activity reflects typical precipitation organization near Kwajalein. Using Kwajalein rain gauges, Schumacher and Houze (2000) found that 75% of Kwajalein rain events lasted less than 30 min and accumulated less than 5 mm.

Objective blob analysis also reflected the preponderance of isolated cells. Using all Kelvin and MRG radar volumes, the modal number of blobs in a given radar scan (radius=157 km) was between 20 and 50, with a larger modal number of blobs for MRG than Kelvin (Fig. 14, Table 6). The modal distance between each blob and its nearest neighboring blob was less than 20 km, indicating that the isolated cells were generally closely scattered.

About 73% of blobs had rain areas smaller than 100 km² (Fig. 15a), compared to about 61% found by Cetrone and Houze (2006) using visual rectangular fitting on their KWAJEX data subset. This difference between our study and Cetrone and Houze (2006) may not be significant given differences in methodology. The mean Kelvin blob rain area was 329 km², compared to 291 km² for MRG, indicating that Kelvin blobs tended to be larger than MRG blobs. The mean length scale of blobs in our dataset was 25 km, which is larger than the mean feature length of 17 km noted over the tropical and subtropical oceans using the Tropical Rainfall Measuring Mission (TRMM) satellite precipitation radar (PR, Nesbitt et al. 2006). This difference with the PR sensor is likely due to our assigned reflectivity threshold of 15 dBZ within 4 km² pixel areas compared to the 17 to 18 dBZ reflectivity detection threshold and 25 km² pixel areas inherent in the PR.

The propensity of small rain blobs indicates that while the regions of convection associated with these wave troughs were by definition synoptically organized, the precipitation within the convective regions was often disorganized on the mesoscale. The typically fewer but larger

blobs per radar scan for Kelvin suggests that Kelvin mesoscale precipitation areas tended to be slightly more organized than those of MRG.

b. Medium-sized and MCS activity

MRG troughs more often contained medium-sized blobs than Kelvin troughs – 25% occurrence for MRG half-hour scans showing activity compared to 16% for Kelvin (Fig. 13, Table 5). However, Kelvin medium-sized blobs more often reached large sizes than MRG, with 11% of Kelvin medium-sized blobs covering at least 20% of the radar domain ($\geq 15\,350\text{ km}^2$) compared to only 6% for MRG.

MCSs are important in Kwajalein rain production. Using tropics-wide rainfall estimations from the TRMM PR and a 100 km length scale criterion for MCSs, Nesbitt et al. (2006) found that MCSs are responsible for 50 to 60% of rainfall near Kwajalein (estimated from their Fig. 11). We used the radar volumes (radius=157 km) to identify times of MCS activity. To compare trough MCS activity to MCS activity outside of these troughs, we also noted the total rain areas in the long-range scan dataset (radius=240 km) corresponding to these MCS times. Among the long-range radar scans available for our trough dataset, at least 75% of the scans that contained rain areas larger than 29% of the long-range scan domain also contained MCSs in the smaller radar volume domain. About 23% of trough long-range scans reached this area threshold, compared to only 5% of long-range scans outside of these troughs. This indicates that Kelvin and MRG wave troughs are preferred locations of MCSs compared to outside the troughs.

MCSs contributed 43% of the rain area accumulated across all Kelvin radar volumes and 28% for MRG. Kelvin MCSs, 40% of which had rain areas covering at least 20% of the radar domain ($\geq 15\,350\text{ km}^2$), were more frequently larger than MRG MCSs, of which only 19%

reached the same area threshold. At least one MCS occurred during 23% of all Kelvin and MRG radar scans, and during 18 of 23 Kelvin events and 14 of 16 MRG events. Recall that when an MCS also qualifies as a convective line, we only note it as a convective line.

The individual wave trough events, however, had no preferred or typical time periods of MCS activity. Seven trough events contained no MCS activity in the 30-min scans, while 61% of scans in one Kelvin event contained MCS activity. Thus, while satellite data show that MRG and Kelvin troughs are coupled with large areas of anomalously cold clouds, these troughs are not always associated with large contiguous areas of precipitation.

There are a number of possible reasons for this MCS variability. Given that we use the Wheeler and Kiladis (1999) spectral analysis method on twice-daily OLR data, we are essentially ignoring any possible cloudiness morphologies between these observation times. Also, we identify wave trough activity using strong wave-filtered negative OLR anomalies averaged across a spatial domain. At times, the strong OLR signal may cover enough of the averaging domain to be considered a wave event but not actually cover the radar domain itself. This was the case for five trough events (Kelvin event numbers 8, 13, and 14, MRG events 7, 13 – Fig. 13). We retain these events in our dataset to minimize subjectivity and to remain consistent with how many previous studies identified wave activity.

The large-scale forcing associated with Kelvin and MRG waves may also vary widely across the trough and from one trough to the next. Other forcings, such as other equatorial waves, the diurnal signal, and dynamics waves from nearby MCSs (e.g., Mapes 1993; Madden and Julian 1994; Chen and Houze 1997), likely modulate convection near Kwajalein and help to produce rain events that often contain isolated convective activity. Also, as was the view of S06, the coupling of waves with convection likely generates MCSs that move quasi-independently from

the wave due to their own dynamics and do not live entirely within the trough regions we examine.

1) MCS EMBEDDED CONVECTION AND POROSITY

MCSs near Kwajalein rarely contained linear features but instead were often visibly disorganized and contained many embedded convective cores throughout their rain field. A visual browsing of TOGA COARE data (Yuter et al. 1995) revealed similar characteristics for MCSs in the west Pacific warm pool.

Many Kwajalein and TOGA COARE MCSs also contained small but noticeable areas where low-level reflectivity was weak surrounded by convective or stratiform reflectivities (e.g., dark blob in Fig. 9f, where these reflectivity holes are evident as white areas within the dark blob). We define this as MCS porosity. MCS porosity did not correlate well with MCS rain area (Fig. 16). The porosity of the MCS in Figure 9f is 0.089, meaning about 9% of the area encompassed by that MCS contained weak reflectivities. The porosity of this MCS totals 1039 km².

About 18% of Kelvin MCSs and 12% of MRG MCSs had porosities greater than 0.05 (Fig. 16). While most porosity fraction values were small, a porosity as small as 0.05 within an MCS that covers 10 000 km² amounts to a cumulative ‘hole’ area of 500 km². This porosity area is significant considering that 92% of blobs in our analysis had rain areas smaller than 500 km². Of all Kelvin MCSs, 35% had hole areas totaling at least 500 km², compared to 15% of MRG MCSs. In terms of the porosity fraction, the most porous MCS was during a Kelvin event – 0.29 porosity, with a 42 047 km² area within MCS perimeter, a 29 664 km² MCS rain area, and a 12 403 km² porosity area.

Holes within the stratiform and convective precipitation fields, as well as scattered convec-

tive cores embedded in the stratiform precipitation field, may have important dynamical and thermodynamical implications. Rather than a leading linear convective feature seeding an expansive trailing stratiform area, as presented in the idealized schematic in Fig. 20a (based on Fig. 1c from Leary and Houze 1979 during the the Global Atmospheric Research Program Atlantic Tropical Experiment (GATE)), we instead appear to have many smaller, embedded convective areas whose collective impact fails to thoroughly seed the entire cloudy region, as shown in Fig. 20b. We also see with the stratiform CFADs of our trough dataset (Fig. 17c,f) and of the S06 dataset (Fig. 18c,f) that there is generally little to no new hydrometeor growth in the stratiform regions of our datasets. This is indicated by the upright structure of these CFADs, as compared to much more active vapor deposition and aggregation processes in, for example, an active Kansas-Oklahoma case shown in Yuter and Houze (1995) (Fig. 19, from the Oklahoma-Kansas Preliminary Regional Experiment for the Stormscale Operational and Research Program - Central Phase).

These stratiform region heterogeneities are not indicated in typical MCS schematics (e.g., Fig. 13 of Zipser 1977; Fig. 1 of Houze et al. 1989). Such schematics average away smaller-scale perturbations and indicate large areas of non-porous precipitation and continuous flow fields that are often not present in tropical MCSs.

Thus, while small, isolated activity dominates the convective activity near Kwajalein during and in the absence of significant Kelvin and MRG troughs, MCSs occur often and contribute a large proportion of total rain area and rainfall. Kelvin and MRG troughs may often be a preferred location for MCSs near Kwajalein, though the amount of MCS activity varies widely from one wave event to the next and MCS structures often have stratiform region heterogeneities. A tendency for larger MCSs during Kelvin events than during MRG events leads

Kelvin MCSs to contribute a larger proportion of Kelvin trough total rain area and suggests that the mesoscale precipitation structures during Kelvin trough events are often slightly more organized than during MRG events.

c. Linear activity

In troughs of both wave types, clearly identifiable linear convective structures were infrequent. For all radar scans, the frequency distribution of blob aspect ratio was Gaussian with a mean near 0.6, meaning the average blob was about 1.7 times longer than it was wide (Table 6). Cetrone and Houze (2006) determined blob aspect ratios near Kwajalein using only the blobs in their dataset that were sufficiently elongated to visually determine orientation. As such, they only considered the 85% of their blobs that had aspect ratios less than 0.66. In our trough dataset, 43% of our blobs had aspect ratios less than 0.66. Cetrone and Houze (2006) found an average aspect ratio of 0.41 for their blob subset, compared to an average near 0.5 when we subset our data using the same criteria.

Using visual classification, 9% of Kelvin scans had convective lines, compared to only 3% of MRG scans, amounting to 24 individual lines during Kelvin events and six during MRG events. Lines were typically less than 150 km long and existed an average of about 2 h within the radar domain (radius=157 km). Six Kelvin lines and three of MRG lines had trailing-stratiform structures. This contrasts with observations in many midlatitude regions. For example, only 3 of 88 convective lines observed by Parker and Johnson (2000) in the central United States did not have trailing, leading, or parallel stratiform structures.

As with ubiquitous isolated activity, the low frequency of linear organization and associated stratiform region implies an overall lack of strong mesoscale organization during both wave

types. However, convective lines occur three times more often during Kelvin radar volumes than during MRG radar volumes, implying that the mesoscale precipitation structures in our sample of Kelvin troughs were frequently slightly more organized than those of MRG.

1) CORRELATION BETWEEN CONVECTIVE LINES AND VERTICAL SHEAR

Vertical wind shear is often used in the midlatitudes to help diagnose the potential for organized convection (e.g., Rotunno et al. 1988) and to explain convective line orientation (e.g., Robe and Emanuel 2001). We examined the closest sounding in time to when each line was at peak visible organization. The resulting shear distributions were not sensitive to whether we used the closest sounding in time or the sounding prior to each line.

The frequency distributions of low-level (1000-700 hPa) vertical wind shear speed and direction for all 59 Kelvin soundings and all 33 MRG soundings (Fig. 21b), independent of convective lines, were similar to the shear frequency distributions of the entire 1999-2003 rainy season dataset (Fig. 21a). The vertical shear distribution when lines were observed – 25 Kelvin soundings, 5 MRG soundings (Fig. 21c) – was also similar to the 1999-2003 superset. There was some indication that sheer speed during Kelvin troughs and during Kelvin convective lines was often slightly stronger than during MRG troughs, MRG lines, and during typical Kwajalein observations. Given that Kelvin wave amplitudes tend to be larger than MRG amplitudes, we would generally expect stronger vertical wind shears in a Kelvin wave environment compared to MRG. However, the small sample size of trough soundings and convective line soundings makes the significance of this observation uncertain. Also, it is difficult to quantify any dynamical significance from these vertical wind shears because we do not account for the location of each particular sounding with respect to the trough axis. Low- and upper-level wind signals

vary widely based on equatorial wave phase.

Cetrone and Houze (2006) noted strong preferences in their KWAJEX data for rain echoes to align northeast-southwest or northwest-southeast. These orientations were often parallel or normal to the low-level shear vector, as was also noted in GATE and TOGA COARE (e.g., Barnes and Sieckman 1984; LeMone et al. 1998). In our dataset, there was no strongly preferred blob azimuthal orientation among all rain blobs across all radar scans. Our convective lines did not distinctly prefer the orientations noted in Cetrone and Houze (2006) (Table 5).

Vertical wind shear was often poorly correlated with line orientation in our Kelvin and MRG trough dataset near Kwajalein. LeMone et al. (1998) found that different combinations of weak ($< 4 \text{ ms}^{-1}$) and strong low-level (1000-800 hPa) and mid-level (800-400 hPa) shears were linked to specific orientations of convective lines during TOGA COARE. These results were augmented by Johnson et al. (2005) during the South China Sea Monsoon Experiment (Fig. 22). Johnson et al. (2005) noted that these observed orientation preferences have also been found in numerical modeling experiments in other locations (e.g., Robe and Emanuel 2001). We interpreted Figure 22 rather liberally, with conditions of parallel or perpendicular between low- and mid-level shear, and line orientations with respect to low- and mid-level shear, set at $\pm 20^\circ$. Only 6 of 29 available line-sounding pairs (one Kelvin line was missing sounding data) followed this schematic. When angle conditions were relaxed to 30° , only nine pairs matched.

6. Convective and stratiform precipitation structures

The differences between Kelvin and MRG troughs in the distributions of convective and stratiform precipitation areas were similar to the differences in total precipitation area (Chapter

4). Kelvin troughs tend to have larger convective and stratiform precipitation areas than those of MRG troughs. Using convective-stratiform partitioning, we can estimate the distributions of rainfall amounts from our Kelvin and MRG trough data. We used an average rain rate of $0.525 \text{ mmhr}^{-1}\text{km}^{-2}$, which was noted during KWAJEX (Yuter et al. 2005) and was nearly identical to conditional rain rate observations during TOGA COARE (Short et al. 1997), and a 3:1 convective-to-stratiform rainrate ratio noted during TOGA COARE (Yuter and Houze 1998). We found that Kelvin troughs tend to be rainier than MRG troughs, reflecting that Kelvin convective and stratiform areas tended to be larger than those of MRG troughs.

a. Stratiform precipitation area

Total rain area and stratiform rain area were expectedly highly correlated (Fig. 23). Since Kelvin trough rain areas tended to be larger than those of MRG, Kelvin trough stratiform rain areas tended to be larger (Table 7). About 8% of Kelvin stratiform rain areas exceeded 33% of the radar domain ($> 25\,584 \text{ km}^2$), compared to 4% for MRG. In the S06 dataset, Kelvin stratiform areas still tended to be larger than MRG stratiform areas but the difference was smaller than with our trough dataset – 7% of S06 Kelvin stratiform areas exceeded 33% of the radar domain compared to 6% for S06 MRG. This confirms the suggestion in S06 that Kelvin-associated rain areas tend to have larger stratiform rain areas than those of MRG, but this difference was slightly more pronounced when only the wave troughs were considered.

b. Stratiform precipitation area fraction

The proportion of total precipitation area that is stratiform is called ‘stratiform area fraction’. This is a useful statistic because the proportion of precipitation that is stratiform affects large-scale divergence and latent heating and momentum profiles (Mapes and Houze 1995) and because the precipitation dynamics affect rainfall amounts.

Stratiform precipitation contributed about 0.77 of the total wave type-accumulated rain area for both wave types in our dataset and in the S06 dataset, and stratiform and weak precipitation echoes together contributed near 0.82. Schumacher and Houze (2000), using all radar volumes during Aug. 1998-Aug. 1999, found that stratiform area made up 0.86 of the total accumulated rain area near Kwajalein. This discrepancy with our results is likely due to their requirement of ‘significant’ precipitation. As a point of reference, the stratiform area proportion of accumulated total areas in this study is very similar to observations during the East Pacific Investigation of Climate Processes in the Coupled Ocean-Atmosphere System (EPIC, 76%, Cifelli et al. 2007), less than during TEPPS (84%, Cifelli et al. 2007), and more than during TOGA COARE ship cruises (66%-74%, Short et al. 1997). These differences in stratiform area fraction may not be significant given differences in methodology among these studies.

The stratiform area fractions of small total rain areas varied widely (Fig. 24). As total rain areas increased, the variance of stratiform area fractions decreased as fractions converged to 1.0. This creates a well-defined separation between observed and unobserved stratiform area fractions for a given total rain area. This relationship between stratiform area fraction and total area reflects the strong correlation of total area with stratiform area (noted in Section a) and the poor correlation of total area with convective area (noted ahead in Section c). Small total rain areas imply small rain blobs, and these small blobs often have much smaller stratiform

proportions than larger blobs. The S06 dataset produced similar results, which suggests that this statistic is robust.

c. Convective precipitation area

In addition to quantifying total precipitation areas and stratiform proportions, it is also important to quantify the total area containing the distinct dynamics and rather intense rainfall of the convective regime. We can also observe the maximum observed area of convective precipitation within our wave datasets.

Convective rain area was not well correlated with total rain area (e.g., Yuter and Houze 1998). Increases in total rain area outpaced increases in convective rain area by greater amounts as total area increased (Fig. 25). Like stratiform area fraction, the distributions of convective area were very similar between the two wave types (Table 7).

Convective precipitation area was never observed to exceed about 20% of the radar domain (about 15 684 km²). This maximum convective area occurred with a total rain area of about 33 000 km² (44% of the radar domain) and is similar to results observed during TOGA COARE (Yuter and Houze 1998). This peak in observed convective rain area was nearly 5000 km² greater for Kelvin than MRG using both the current and S06 datasets. A total of about 50 radar volumes within two of our Kelvin trough events reached and sustained convective rain areas greater than any observed for MRG. Convective areas corresponding to the 0.75 and 0.9 cumulative frequency percentiles were slightly larger for Kelvin data than MRG data (Table 7). For the 8% of Kelvin radar volumes and 1% of MRG radar volumes with total rain areas exceeding 33 000 km², the maximum observed convective rain decreased as a function of total area.

A tendency for slightly larger total convective areas during Kelvin trough events than MRG events are supported by results from Wheeler et al. (2000). Through a 17 year composite of reanalysis data, their Figures 7 and 15 (reproduced as our Figs. 26 and 27) suggest that convectively-coupled Kelvin waves are associated with deeper and perhaps stronger updrafts, and thus more enhanced convergence through this tropospheric column, than those of MRG waves. The updraft region also appears to be more persistent in time with respect to the wave-filtering base point.

Because these convective area limits were observed with both our trough dataset and the S06 wave dataset, and because the TOGA COARE aircraft also observed a similar maximum achieved convective area, these results appear to be robust. These limits suggest a maximum area of convective precipitation that the atmosphere near Kwajalein can sustain, though the physical reasons for this should be a subject of future research.

d. Vertical reflectivity distributions and precipitation intensity

The vertical patterns of reflectivity distribution – the CFAD shapes – were very similar between the ensembles of Kelvin and MRG trough data (Fig. 17). The near-vertical structure of the stratiform CFADs indicates little new stratiform precipitation growth. However, the modal near-surface and mid-level convective and stratiform reflectivity modes were 3 to 4 dB larger for our Kelvin troughs than MRG. The typical radar calibration uncertainty is ± 2 dB, and half of our radar volumes were not calibrated. A 3 to 4 dB modal reflectivity offset would be significant assuming calibration offset values would be randomly distributed among the uncalibrated volumes, but this assumption is likely not true. Also, blob reflectivity calculations do not reflect the CFAD reflectivity difference (Table 6), suggesting that this difference may be insignificant.

S06 noted with their wave events that the near-surface mode of Kelvin total reflectivity distribution was 1 to 2 dB weaker than with MRG (Fig. 18a,d). When we partitioned the S06 data into convective and stratiform precipitation, their Kelvin and MRG radar ensembles had nearly identical convective CFADs and stratiform CFADs (Fig. 18 b,c,e,f), indicating that the reduced modal reflectivities in the total Kelvin CFAD were due to slightly larger stratiform areas rather than strong differences with MRG in convective and stratiform structure and intensity. These slightly larger S06 Kelvin stratiform rain areas were discussed in Section a (Fig. 23). The modal reflectivity differences between S06 Kelvin and S06 MRG CFADs are within the radar calibration uncertainty and may be insignificant.

A different time span for the data record in S06, leading to differences in radar calibrations from our data record, as well as the different definitions of wave-related rain events in S06, may explain the differences between the S06 wave event CFADs and our trough event CFADs. In either case, both datasets show a tendency for slightly larger stratiform areas for Kelvin events than MRG, confirming the S06 finding.

e. Effective echo heights

Most precipitating clouds at Kwajalein are mixed. The freezing level height is near 4.5 km altitude (Yuter et al. 2005) and the echo top height mode is near 7 km altitude. The effective echo height calculation revealed nearly identical effective echo height distributions for Kelvin and MRG troughs and for convective and stratiform precipitation subsets (Fig. 28). Here, similar to Yuter (2004) results during TEPPS and TOGA COARE, the variance in convective and stratiform effective echo height decreased with increasing convective and stratiform area. Total rain areas larger than 10 000 km² always containing echo heights above 5 km altitude. Data

from GATE (Houze and Cheng 1977) and from 13 sampled days during KWAJEX (Cetrone and Houze 2006) contained a positive but scattered relationship between rain area and echo height which was not found here.

7. Summary: The mesoscale precipitation characteristics of equatorial wave troughs

The Kelvin and MRG wave trough events represent a subset of Kwajalein rain events that often contain horizontally larger precipitation areas compared to typical Kwajalein rain areas (Table 4), implying enhanced rainfall amounts due to increased rain duration during trough events. This is consistent with Reed and Recker (1971), who studied 18 tropical synoptic waves in the west Pacific region from the Marshall Islands westward about 10° longitude and found that the wave troughs had higher rainfall accumulations. As such, Kelvin and MRG troughs are generally preferred locations for MCSs compared to longer-term precipitation data at Kwajalein (Tables 4 and 5, Fig. 13).

However, the number of radar volumes containing MCS activity varied widely among the trough events (Fig. 13), and nearly half of the radar volumes in our Kelvin and MRG wave troughs consisted only of small, isolated areas of precipitation (Tables 5 and 6, Figs. 13, 14, and 15a). Thus, while satellite data show that MRG and Kelvin troughs are coupled with large areas of anomalously cold clouds, these troughs are not always associated with large contiguous areas of precipitation. Two of the possible reasons for this are linked to our definition of trough events: (1) the widely used Wheeler and Kiladis (1999) spectral analysis method uses twice-daily OLR data, and the large-scale cloudy areas may at times be discontinuous between the twice-daily

satellite times; (2) we look for strong wave-filtered negative OLR anomalies averaged across a spatial domain to identify strong trough convective activity, so in some cases the strong OLR signal can be situated outside of the Kwajalein radar domain but is considered an event across the averaging domain. This was the case for five trough events (Kelvin event numbers 8, 13, and 14, MRG events 7, 13 – Fig. 13). Our methodology identifies these time periods as trough events in the averaging box, and we retain these events in our dataset to minimize subjectivity and to remain consistent with how many previous studies identified wave activity. These five events had rain areas that were generally smaller than most of the other wave events, and three events contained only isolated activity.

Kelvin and MRG waves may also not be providing enough large-scale forcing consistently across the whole trough region to sustain MCSs. Other significant forcings, such as other equatorial waves, the diurnal signal, and gravity waves from nearby MCSs (e.g., Mapes 1993; Madden and Julian 1994; Chen and Houze 1997), likely modulate convection near Kwajalein and help to produce rain events that often contain isolated convective activity.

It is also likely that the interaction of waves with convection generates MCSs that, due to their own dynamics, move at different velocities than the wave. MCSs can then decouple somewhat from the wave trough and move quasi-independently. This was the view of S06, though our trough-related approach in this study does not account for such independent MCS motion.

Observed MCS structure near Kwajalein also contrasts with MCS schematics (e.g., Fig. 1 of Houze et al. 1989; Fig. 13 of Zipser 1977). These schematics are the result of compositing MCS structures across many times and depict continuous air and moisture flow fields across an expansive, non-porous cloud region. MCSs in this study rarely corresponded to this averaged

structure because they usually had many convective cores embedded throughout the stratiform area and had internal areas where reflectivity did not exceed 15 dBZ (e.g., Table 6, Fig. 16). This was also observed when we browsed TOGA COARE data (Yuter et al. 1995). Embedded convective cores and reflectivity holes suggest that small-scale perturbations exist within the MCSs and interrupt flow fields in ways that may be dynamically significant, and that such perturbations are more abundant and/or stronger in Kelvin MCSs than in MRG.

Samples over both wave types had observed maximum attained convective precipitation areas, both overall and for a given total precipitation area. This suggests a lid on the size of convective precipitation sustainable by the atmosphere near Kwajalein. Stratiform precipitation area fractions varied widely with small total rain areas but generally increased and converged towards 1.0 as total precipitation areas increased. These convective and stratiform precipitation area properties were also observed using the S06 dataset, suggesting that they are robust results.

Kelvin trough events often contained slightly more organized mesoscale precipitation structures than MRG trough events. Across the whole dataset, Kelvin troughs more often contained fewer but larger contiguous rain blobs, larger MCSs, and larger total precipitation areas than MRG troughs (Tables 5, 6, and 7, Figs. 12, 14, and 15b,c). Convective lines occurred three to four times more often during Kelvin troughs than MRG (Table 5, Fig. 13).

Investigation of the detailed physical reasons for differences in mesoscale precipitation organization between Kelvin and MRG waves was beyond the scope of this study. The spatiotemporal resolution of our observations does not allow for such an examination. Few previous equatorial wave studies have performed wave-related dynamical analyses that allow for direct comparisons of dynamical features of different wave types. Wheeler et al. (2000), for example, detailed the horizontal and vertical characteristics of the various types of convectively-coupled

waves identified across January 1979 through August 1996. Much of their analysis, however, relied on reanalysis output, which can be unreliable over the open oceans due to sparse data.

If we were to examine dynamics during our trough events using reanalysis, our results should be very similar to those found by Wheeler et al. (2000). Their Figures 7 and 15 (reproduced as our Figs. 26 and 27) suggest that convectively-coupled Kelvin waves have associated with them deeper and perhaps stronger areas of upward motion than those of MRG waves. The region of upward motion also seems to be more persistent in time with respect to the filtering base point. Such an enhanced region of positive vertical motion implies enhanced convergence through at least some of the troposphere for the Kelvin wave compared to the MRG wave. This may be expected given that Kelvin wave amplitudes are generally larger than MRG wave amplitudes.

The direction of motion of the large-scale convergence region may also impact wave dynamics and convective development. Haertel and Johnson (2000) used a dry linear modeling study to show that while a thermal forcing produces local-scale perturbations in opposite directions, a moving thermal forcing creates a stronger gravity mode response in its direction of motion. With the eastward-moving Kelvin wave, the eastward-moving convective region may enhance wave structure and convective activity more strongly to its east where new convective development occurs, thus preconditioning the upstream convective environment (Straub and Kiladis 2003a). However, since the MRG convective region moves westward, an enhanced gravity mode response may enhance the wave structure towards the west, rather than towards the east where the new convective development occurs.

8. Concluding Remarks

In this study, we have used several techniques to analyze the mesoscale precipitation structures associated with large-scale equatorial waves near Kwajalein Atoll. These techniques include: visual organization analysis (identifying isolated activity, MCSs, and convective line structures – Table 5, Fig13), upper-air sounding composites (Figs. 11 and 21), objective contiguous rain area ‘blob’ analysis (identifying number, size, shape, orientation, separation, and intensity of individual rain blobs – Table 6, Figs. 9, 14, 15, and 16), convective-stratiform precipitation classification (Table 7, Figs. 9, 17, 18, 24, 25, and 28), total rain area coverage (Tables 4 and 7, Figs. 12 and 13), contoured frequency-by-altitude reflectivity diagrams (Figs. 17 and 18), and effective echo height distributions (Fig. 28).

The main results – descriptions of the mesoscale precipitation structures associated with Kelvin and MRG troughs – are outlined in Section 7. In comparing the statistics of radar volumes during our Kelvin samples to those during MRG, we found that the Kelvin troughs tended to have larger total rain areas and larger stratiform rain areas compared to MRG. This conclusion is consistent with the speculation of S06 based on their CFAD analysis, though the shift in the CFAD reflectivity mode which led S06 to make this speculation is not robust to our change in wave event definition. As speculated by S06, Kelvin troughs tended to have more organized convection than MRG, with more frequent occurrences of linear structures. Besides these arguably modest differences, the convection occurring in the two types of wave troughs does not differ significantly.

Some of our results are consistent with previous studies of tropical precipitation. Longer time-scale studies have noted the propensity of Kwajalein rain events to contain scattered areas of isolated precipitation (e.g., Schumacher and Houze 2000; Yuter et al. 2005; Cetrone and

Houze 2006). The skewed lognormal frequency distributions of total precipitation areas and of individual contiguous precipitation areas during our trough events (Table 7, Figs. 12 and 15a), which reflect the propensity of small and isolated precipitation activity, are consistent with previous studies at Kwajalein and elsewhere in the tropics (e.g., Houze and Cheng 1977; López 1977; Yuter et al. 2005; Cetrone and Houze 2006). Also, the stratiform area proportion of accumulated total areas in this study (about 77%) is very similar to observations during EPIC (76%, Cifelli et al. 2007), less than during TEPPS (84%, Cifelli et al. 2007), and more than during TOGA COARE ship cruises (66%-74%, Short et al. 1997). These differences in stratiform area fraction may not be significant given differences in methodology among these studies.

A result that was inconsistent with other studies (e.g., Barnes and Sieckman 1984; LeMone et al. 1998; Johnson et al. 2005; Cetrone and Houze 2006) was the poor correlation of convective line orientation to low- and mid-level vertical wind shear (Table 5, Fig. 21c). This may warrant further investigation where convective lines occur more frequently and can be observed across a larger domain than that of the Kwajalein radar and with a spatiotemporally denser sounding network.

The generality of these findings with these and other types of waves should be investigated in other tropical regions where long term radar datasets exist. Other methods of identifying equatorial waves (e.g., relying more closely on the horizontal structure functions of equatorial wave theory, as in Yang et al. 2003) and their associated mesoscale precipitation organization may also be interesting to test. Objective blob analysis may be useful in quantifying the horizontal characteristics of individual rain areas (Table 6), while the volume-wide effective echo height calculation may be a more useful representation of storm heights than following particu-

lar reflectivity contours (Fig. 28). The results of many of the statistical analyses of precipitation structures that we employ, especially the ensemble thresholds of convective and stratiform precipitation structures (Figs. 24, 25), would be convenient to compare to model output . It may be useful to quantify MCS embedded convection and MCS porosity in other regions, study their physical implications, and evaluate the realism of modeled MCSs.

Bibliography

Barnes, G. M. and K. Sieckman, 1984: The environment of fast- and slow-moving tropical mesoscale convective cloud lines. *Mon. Wea. Rev.*, **112**, 1782–1794.

Cetrone, J. and R. A. Houze, 2006: Characteristics of tropical convection over the ocean near Kwajalein. *Mon. Wea. Rev.*, **134**, 834–853.

Chen, S. S. and R. A. Houze, 1997: Diurnal variation and life–cycle of deep convective systems over the tropical Pacific warm pool. *Quart. J. Roy. Meteor. Soc.*, **123**, 357–388.

Cifelli, R., S. W. Nesbitt, S. A. Rutledge, W. A. Petersen, and S. Yuter, 2007: Radar characteristics of precipitation features in the EPIC and TEPPS regions of the East Pacific. *Mon. Wea. Rev.*, **135**, 1576–1595.

DeMott, C. A. and S. A. Rutledge, 1998: The vertical structure of TOGA COARE convection. Part II: modulating influences and implications for diabatic heating. *J. Atmos. Sci.*, **55**, 2748–2762.

Dunkerton, T. J., 1993: Observation of 3–6–day meridional wind oscillations over the tropical Pacific, 1973–1992: Vertical structure and interannual variability. *J. Atmos. Sci.*, **50**, 3292–3307.

Dunkerton, T. J. and M. P. Baldwin, 1995: Observation of 3–6–day meridional wind oscillations

- over the tropical Pacific, 1973–1992: Horizontal structure and propagation. *J. Atmos. Sci.*, **52**, 1585–1601.
- Gill, A. E., 1980: Some simple solutions for heat-induced tropical circulation. *Quart. J. Roy. Meteor. Soc.*, **106**, 447–462.
- Grabowski, W. W., 2003: MJO-like coherent structures: sensitivity simulations using the cloud-resolving convective parameterization (CRCP). *J. Atmos. Sci.*, **60**, 847–864.
- , 2004: An improved framework for superparameterization. *J. Atmos. Sci.*, **61**, 1940–1952.
- Gruber, A., 1974: The wavenumber-frequency spectra of satellite-measured brightness in the tropics. *J. Atmos. Sci.*, **31**, 1675–1680.
- Haertel, P. T. and R. H. Johnson, 2000: The linear dynamics of squall line mesohighs and wake lows. *J. Atmos. Sci.*, **57**, 93–107.
- Hayashi, Y., 1982: Space-time spectral analysis and its applications to atmospheric waves. *J. Meteor. Soc. Japan*, **60**, 156–171.
- Hendon, H. H. and B. Liebmann, 1991: The structure and annual variation of antisymmetric fluctuations of tropical convection and their association with Rossby-gravity waves. *J. Atmos. Sci.*, **48**, 2127–2140.
- Houze, R. A., 1997: Stratiform precipitation in regions of convection: A meteorological paradox?. *Bull. Amer. Meteor. Soc.*, **78**, 2179–2196.
- , 2004: Mesoscale convective systems. *Rev. Geophys.*, **42**, RG4003.

- Houze, R. A., S. Brodzik, C. Schumacher, S. E. Yuter, and C. R. Williams, 2004: Uncertainties in oceanic radar rain maps at Kwajalein and implications for satellite validation. *J. Appl. Meteor.*, **43**, 1114–1132.
- Houze, R. A., S. S. Chen, D. E. Kingsmill, Y. Serra, and S. E. Yuter, 2000: Convection over the Pacific warm pool in relation to the atmospheric Kelvin-Rossby wave. *J. Atmos. Sci.*, **57**, 3058–3089.
- Houze, R. A. and C. Cheng, 1977: Radar characteristics of tropical convection observed during GATE: Mean properties and trends over the summer season. *Mon. Wea. Rev.*, **105**, 964–980.
- Houze, R. A., S. A. Rutledge, M. I. Biggerstaff, and B. F. Smull, 1989: Interpretation of Doppler weather-radar displays in midlatitude mesoscale convective systems. *Bull. Amer. Meteor. Soc.*, **70**, 608–619.
- Johnson, R. H., S. L. Aves, P. E. Ciesielski, and T. D. Keenan, 2005: Organization of oceanic convection during the onset of the 1998 East Asian summer monsoon. *Mon. Wea. Rev.*, **133**, 131–148.
- Johnson, R. H. and X. Lin, 1997: Episodic trade wind regimes over the western Pacific warm pool. *J. Atmos. Sci.*, **54**, 2020–2034.
- Khairoutdinov, M., D. Randall, and C. DeMott, 2005: Simulations of the atmospheric general circulation using a cloud-resolving model as a superparameterization of physical processes. *J. Atmos. Sci.*, **62**, 2136–2154.
- Kiladis, G. N., G. A. Meehl, and K. M. Weickmann, 1994: Large-scale circulation associated with westerly wind bursts and deep convection over the western equatorial Pacific. *J. Geophys. Res.*, **99**.

- Kleeman, R., 1989: A modeling study of the effect of the Andes on the summertime circulation of tropical South America. *J. Atmos. Sci.*, **46**, 3344–3362.
- Kuang, Z., P. N. Blossey, and C. S. Bretherton, 2005: A new approach for 3d cloud-resolving simulations of large-scale atmospheric circulation. *Geophys. Res. Lett.*, **32**, L02 809.
- Leary, C. A. and R. A. Houze, 1979: The structure and evolution of convection in a tropical cloud cluster. *J. Atmos. Sci.*, **36**, 437–457.
- LeMone, M. A., E. J. Zipser, and S. B. Trier, 1998: The role of environmental shear and thermodynamic conditions in determining the structure and evolution of mesoscale convective systems during TOGA COARE. *J. Atmos. Sci.*, **55**, 3493–3518.
- Liebmann, B. and C. A. Smith, 1996: Description of a complete (interpolated) outgoing long-wave radiation dataset. *Bull. Amer. Meteor. Soc.*, **77**, 1275–1277.
- Lin, X. and R. H. Johnson, 1996: Heating, moistening, and rainfall over the western Pacific warm pool during TOGA COARE. *J. Atmos. Sci.*, **53**, 3367–3383.
- Lindzen, R. S., 1967: Planetary waves on beta planes. *Mon. Wea. Rev.*, **95**, 441–451.
- Lindzen, R. S. and T. Matsuno, 1968: On the nature of large-scale wave disturbances in the equatorial lower stratosphere. *J. Meteor. Soc. Japan*, **46**, 215–221.
- López, R. E., 1977: The lognormal distribution and cumulus cloud populations. *Mon. Wea. Rev.*, **105**, 865–872.
- Madden, R. A. and P. R. Julian, 1994: Observations of the 40–50-day tropical oscillation—a review. *Mon. Wea. Rev.*, **122**, 814–837.

- Magaña, V. and M. Yanai, 1995: Mixed Rossby–gravity waves triggered by lateral forcing. *J. Atmos. Sci.*, **52**, 1473–1486.
- Majda, A. J., B. Khouider, G. N. Kiladis, K. H. Straub, and M. G. Shefter, 2004: A model for convectively coupled tropical waves: Nonlinearity, rotation, and comparison with observations. *J. Atmos. Sci.*, **61**, 2188–2205.
- Mapes, B. E., 1993: Gregarious tropical convection. *J. Atmos. Sci.*, **50**, 2026–2037.
- Mapes, B. E. and R. A. Houze, 1995: Diabatic divergence profiles in western pacific mesoscale convective systems. *J. Atmos. Sci.*, **52**, 1807–1828.
- Matsuno, T., 1966: Quasi-geostrophic motions in the equatorial area. *J. Meteor. Soc. Japan*, **44**, 25–43.
- Medioni, G., M. S. Lee, and C. K. Tang, 2000: *A computational framework for segmentation and grouping*. Elsevier, 260 pp.
- Nesbitt, S. W., R. Cifelli, and S. A. Rutledge, 2006: Storm morphology and rainfall characteristics of TRMM precipitation features. *Mon. Wea. Rev.*, **134**, 2702–2721.
- Nesbitt, S. W., E. J. Zipser, and D. J. Cecil, 2000: A census of precipitation features in the tropics using TRMM: Radar, ice scattering, and lightning observations. **13**, 4087–4106.
- Parker, M. D. and R. H. Johnson, 2000: Organizational modes of midlatitude mesoscale convective systems. *Mon. Wea. Rev.*, **128**, 3413–3436.
- Pires, P., J. L. Redelsperger, and J. P. Lafore, 1997: Equatorial atmospheric waves and their association to convection. *Mon. Wea. Rev.*, **125**, 1167–1184.

- Randall, D., M. Khairoutdinov, A. Arakawa, and W. Grabowski, 2003: Breaking the cloud parameterization deadlock. *Bull. Amer. Meteor. Soc.*, **84**, 1547–1564.
- Reed, R. J. and E. E. Recker, 1971: Structure and properties of synoptic-scale wave disturbances in the equatorial western Pacific. *J. Atmos. Sci.*, **28**, 1117–1133.
- Rickenbach, T. M. and S. A. Rutledge, 1998: Convection in TOGA COARE: Horizontal scale, morphology, and rainfall production. *J. Atmos. Sci.*, **55**, 2715–2729.
- Robe, F. R. and K. A. Emanuel, 2001: The effect of vertical wind shear on radiative-convective equilibrium states. *J. Atmos. Sci.*, **58**, 1427–1445.
- Rotunno, R., J. B. Klemp, and M. L. Weisman, 1988: A theory for strong, long-lived squall lines. *J. Atmos. Sci.*, **45**, 463–485.
- Roundy, P. E. and W. M. Frank, 2004: A climatology of waves in the equatorial region. *J. Atmos. Sci.*, **61**, 2105–2132.
- Russ, J. C., 1995: *The image processing handbook*. CRC Press, Boca Raton, 674 pp.
- Schumacher, C. and R. A. Houze, 2000: Comparison of radar data from the TRMM satellite and Kwajalein oceanic validation site. *J. Appl. Meteor.*, **39**, 2151–2164.
- Short, D. A., P. A. Kucera, B. S. Ferrier, J. C. Gerlach, S. A. Rutledge, and O. W. Thiele, 1997: Shipboard radar rainfall patterns within the TOGA COARE IFA. *Bull. Amer. Meteor. Soc.*, **78**, 2817–2836.
- Slingo, J., P. Inness, J. Strachan, S. Woolnough, and G. Y. Yang, 2007: Systematic errors in the tropics and the role of multi-scale interactions., *3rd WGNE Workshop on Systematic Errors in Climate and NWP Models*, San Francisco, CA, 101.

- Sobel, A. H., S. E. Yuter, C. S. Bretherton, and G. N. Kiladis, 2004: Large-scale meteorology and deep convection during TRMM KWAJEX. *Mon. Wea. Rev.*, **132**, 422–444.
- Steiner, M., J. R. A. Houze, and S. E. Yuter, 1995: Climatological characterization of three-dimensional storm structure from operational radar and rain gauge data. *J. Appl. Meteor.*, **34**, 1978–2007.
- Straub, K. H. and G. N. Kiladis, 2002: Observations of a convectively coupled Kelvin wave in the eastern Pacific ITCZ. *J. Atmos. Sci.*, **59**, 30–53.
- , 2003a: Extratropical forcing of convectively coupled Kelvin waves during Austral winter. *J. Atmos. Sci.*, **60**, 526–543.
- , 2003b: The observed structure of convectively coupled Kelvin waves: Comparison with simple models of coupled wave instability. *J. Atmos. Sci.*, **60**, 1655–1668.
- Swann, A., A. H. Sobel, S. E. Yuter, and G. N. Kiladis, 2006: Observed radar reflectivity in convectively coupled Kelvin and mixed Rossby–gravity waves. *Geophys. Res. Lett.*, **33**, L10 804.
- Takayabu, Y. N., 1994: Large-scale cloud disturbances associated with equatorial waves. Part I: Spectral features of the cloud disturbances. *J. Meteor. Soc. Japan*, **72**, 433–448.
- Wang, B. and X. Xie, 1996: Low-frequency equatorial waves in vertically sheared zonal flow. Part I: stable waves. *J. Atmos. Sci.*, **53**, 449–467.
- Webster, P. and R. Lukas, 1992: TOGA COARE: The Coupled Ocean–Atmosphere Response Experiment. *Bull. Amer. Meteor. Soc.*, **73**, 1377–1416.

- Wheeler, M. and G. N. Kiladis, 1999: Convectively coupled equatorial waves: Analysis of clouds and temperature in the wavenumber–frequency domain. *J. Atmos. Sci.*, **56**, 374–399.
- Wheeler, M., G. N. Kiladis, and P. J. Webster, 2000: Large–scale dynamical fields associated with convectively coupled equatorial waves. *J. Atmos. Sci.*, **57**, 613–640.
- Yang, G.-Y., B. Hoskins, and J. Slingo, 2003: Convectively coupled equatorial waves: a new methodology for identifying wave structures in observational data. *J. Atmos. Sci.*, **60**, 1637–1654.
- Yang, G. Y., B. J. Hoskins, and J. M. Slingo, 2007: Convectively coupled equatorial waves in the Hadley Centre climate models. *3rd WGNE Workshop on Systematic Errors in Climate and NWP Models*, San Francisco, CA, 141.
- Yuter, S. E., 2004: The structure and variability of tropical oceanic precipitation in the western Pacific warm pool and eastern Pacific ITCZ. *3rd European Conf. Radar in Meteorology and Hydrology*, Gotland, Sweden, 99–104.
- Yuter, S. E. and R. A. Houze, 1995: Three–dimensional kinematic and microphysical evolution of Florida cumulonimbus. Part II: Frequency distributions of vertical velocity, reflectivity, and differential reflectivity. *Mon. Wea. Rev.*, **123**, 1941–1963.
- , 1998: The natural variability of precipitating clouds over the western Pacific warm pool. *Quart. J. Roy. Meteor. Soc.*, **124**, 53–99.
- , 2000: The 1997 Pan American Climate Studies Tropical Eastern Pacific Process Study. Part i: ITCZ region. *Bull. Amer. Meteor. Soc.*, **81**, 451–481.

- Yuter, S. E., R. A. Houze, E. A. Smith, T. T. Wilheit, and E. Zipser, 2005: Physical characterization of tropical oceanic convection observed in KWAJEX. *J. Appl. Meteor.*, **44**, 385–415.
- Yuter, S. E., R. A. Houze, B. F. Smull, F. D. Marks, J. R. Daugherty, and S. R. Brodzik, 1995: TOGA COARE aircraft mission summary images: an electronic atlas. *Bull. Amer. Meteor. Soc.*, **76**, 319–328.
- Yuter, S. E., Y. L. Serra, and R. A. Houze, 2000: The 1997 Pan American Climate Studies Tropical Eastern Pacific Process Study. Part II: stratocumulus region. *Bull. Amer. Meteor. Soc.*, **81**, 483–490.
- Zangvil, A., 1975: Temporal and spatial behavior of large-scale disturbances in tropical cloudiness deduced from satellite brightness data. *Mon. Wea. Rev.*, **103**, 904–920.
- Zangvil, A. and M. Yanai, 1980: Upper tropospheric waves in the tropics. Part I: Dynamical analysis in the wavenumber-frequency domain. *J. Atmos. Sci.*, **37**, 283–298.
- , 1981: Upper tropospheric waves in the tropics. Part II: Association with clouds in the wavenumber-frequency domain. *J. Atmos. Sci.*, **38**, 939–953.
- Ziemiański, M. Z., W. W. Grabowski, and M. W. Moncrieff, 2005: Explicit convection over the western Pacific warm pool in the Community Atmospheric Model. **18**, 1482–1502.
- Zipser, E. J., 1977: Mesoscale and convective-scale downdraughts as distinct components of squall-line circulation. *Mon. Wea. Rev.*, **105**, 1568–1589.

List of Figures

- 1 (Matsuno 1966 Fig. 3a) Frequencies as functions of wave number. Thin solid line: eastward propagating inertio-gravity waves. Thin dashed line: westward propagating inertio-gravity waves. Thick dashed line: Wave that is like the Kelvin wave. 72
- 2 (Gill 1980 Fig. 1b) Linear model solution for a heating region symmetric about the equator. The heating source exists at the convergence line just east of the two cyclones. Contours of perturbation pressure are shown (contoured every 0.3), which is negative everywhere. Arrows indicate the velocity field for the lower layer of the model. The Kelvin wave emanates eastward from the heating source, with associated easterly winds, while a planetary wave emanates westward with associated westerlies. 73

- 3 (Straub and Kiladis 2003a Fig. 2) Regressed OLR (shading), 200 hPa streamfunction (contours), and winds (vectors) at lag times noted. These values are based on a -40 Wm^{-2} anomaly in Kelvin wave-filtered OLR at $7.5^\circ\text{N } 172.5^\circ\text{W}$ for the 15 Southern Hemisphere winters 1979-1993. OLR shading is at ± 6 and 15 Wm^{-2} (dark shading is negative), streamfunction contours are every $7.5 \times 10^5 \text{ m}^2\text{s}^{-1}$ (zero contour omitted), and the longest wind vectors correspond to a 10 ms^{-1} wind (only u and v values significant to at least 95% are shown; significance is determined using a local two-sided test to account for correlation and degrees of freedom). 74
- 4 (Wheeler and Kiladis 1999 Fig. 6) The (a) antisymmetric and (b) symmetric OLR power spectra (across January 1979-August 1996, summed across $10^\circ\text{S} - 10^\circ\text{N}$, with base-10 logarithm taken) divided by the background power spectra (arrived at by averaging the individual power spectra and smoothing wavenumber and frequency). Contours less than 1.1 or greater than 1.4 are omitted. Thin lines are the various equatorial wave dispersion curves for the different equivalent depths ($h=8, 12, 25, 50, 90 \text{ m}$). Thick boxes indicate the regions of the wavenumber-frequency domain that are used to filter OLR data for specific wave types. 75

| | | |
|---|--|----|
| 5 | (Wheeler et al. 2000 (a) Figure 6 (b) Figure 14) The theoretical equatorially trapped (a) Kelvin wave solution and (b) MRG wave solution to the linear shallow water equations on an equatorial β -plane (as in Matsuno 1966) for zonal wavenumber 1. Hatching indicates convergence and shading indicates divergence at a 0.6 interval. Unshaded contours are geopotential at a 0.5 interval. Negative contours are dashed and the zero contour is omitted. Vectors indicate wind, and the longest arrow is 2.3 units. Dimensional scales are as in Matsuno (1966). | 76 |
| 6 | (Wheeler et al. 2000 Fig. 3a and Fig. 3e). Geographical distribution of (a) Kelvin-filtered OLR variance and (b) MRG-filtered OLR variance for all seasons across January 1979-August 1996. Contour interval is 15 (Wm^{-2}) ² . A thick X marks the point of maximum variance – in the eastern Indian Ocean for Kelvin, in the west-central Pacific Ocean for MRG. | 77 |

- 7 ((a)Wheeler and Kiladis 1999 Fig. 9b, (b) Wheeler et al. 2000 Fig. 12) (a) Time-longitude section of the OLR anomalies for the Kelvin wave-filtered band for 0600 UTC 1 September 1992 - 0600 UTC 1 March 1993 averaged across 10°S-2.5°N. Solid and dashed lines correspond to convectively coupled Kelvin wave disturbances. (b) Time-longitude diagram of anomalies of OLR (hatching/shading) and 1000 hPa zonal-meridional wind (vector) associated with the OLR variation of the convectively coupled MRG wave at base point 7.5°N 177.5°E. Each field is averaged across 2.5 - 12.5°N. Two levels of hatching denote OLR anomalies greater than 4 and 8 Wm^{-2} , and the three levels of shading denote OLR anomalies less than -4, -8, and -12 Wm^{-2} , respectively. Wind vectors are locally significant to 99%, with the largest vector 0.69 ms^{-1} 78
- 8 Kelvin (a-c) and MRG (d-f) OLR anomaly data for this study. The top row of each wave type is the wave-filtered OLR anomaly data, and the bottom row is the raw OLR anomaly data. Lag times are given as -48 h (a,d), 0 h (b,e), and +48 h (c,f). An X marks the location of Kwajalein. 79

9 Example reflectivity (a,d), convective-stratiform-weak (b,e, see Section 3), and blob detection (c,f, see Section 4) representations of two different organizational regimes in this study – isolated (a-c, 0549 UTC 13 December 2001), and large rain areas with embedded convection (coexistent with some isolated, d-f, 0223 UTC 30 October 1999). These images represent data from the 0-2 km altitude layers of the three-dimensional radar volumes (radius=157 km). Distance scales are in km. Convective-stratiform-weak map colors represent weak echo (light gray), stratiform echo (blue), and convective echo (green). Individual colors on the blob detection represent different individual contiguous rain blobs. The dark MCS blob in (f) is referred to in the text for its porosity, which is 0.089, totals 919 km², and is evident as white space within the blob. 80

10 (Nesbitt et al. 2006 Fig. 1d) TRMM PR near-surface reflectivity (shading, dBZ), TRMM Lightning Imaging Sensor lightning flashes (plus signs), and locations of best-fit ellipses of precipitation features within each scene. The major and minor axes are labeled for the largest precipitation feature. 81

- 11 Time-lag composite sounding anomalies for temperature (a,b), specific humidity (c,d), and zonal wind (e,f). Kelvin and MRG composites for this study (a,c,e) are in 12 h intervals, temporally smoothed for display using a 36 h running mean. Soundings during a TEPPS Kelvin wave event (b,d,f) correspond to Straub and Kiladis (2002) Figs. 10, 14, and 11, respectively, with 4 h resolution. Darker shading and solid contours represent positive values. Contour intervals are: (a) 0.25 °C, no values $<|0.25|$; (b) 0.3 °C, no zero values; (c) 0.125 gkg⁻¹, no values $<|0.125|$; (d) 0.3 gkg⁻¹, no zero values; (e) 0.375 ms⁻¹, no values $<|0.375|$; (f) 1.0 ms⁻¹, no zero values. Areas in (a,c,e) significantly different to 90% (Student's t-test) from the full July-December 1999-2003 dataset are outlined in bold contour. Time scales in (a,c,e) reflect one full ridge-trough-ridge wavelength. The MRG time axis has been reversed because MRG waves move east to west. 82
- 12 Normalized frequency of occurrence of total rain areas across all Kelvin and MRG radar volumes using a reflectivity threshold of 15 dBZ on the 0-2 km altitude layer of radar volumes (radius=157 km, domain area \cong 76 752 km²) and plotted on a logarithmic scale. Dots are placed where Kelvin data have a significantly higher frequency of that particular rain area bin than MRG, and likewise an X is placed along the MRG line where MRG has a significantly higher frequency than Kelvin. Significance is calculated to 95% using a 10 000-member Monte Carlo test. 84

| | | |
|----|---|----|
| 13 | Horizontal precipitation organization for (a) Kelvin radar volumes and (b) MRG volumes in this study, along with observed precipitation areas (bottom of each). Organization is determined visually (Section 3) using half-hour intervals of the 0-2 km altitude layer of radar volumes (radius=157 km, domain area \cong 76 752 km ²); precipitation areas are also extracted at these half-hour intervals. Wave events are bounded by vertical lines, and a point is placed at each time for the type(s) of organization seen at that time. Note that these are not continuous time series. | 85 |
| 14 | Normalized frequency of occurrence of the number of blobs per radar scan (at the 0-2 km altitude layer of radar volumes, radius=157 km) across all Kelvin and MRG radar volumes using a blob reflectivity threshold of 15 dBZ. Statistical significance is indicated as in Fig. 12. | 86 |
| 15 | Normalized frequency of occurrence of (a) all blob sizes, (b) ‘medium-sized’ non-MCS blobs, and (c) MCS blob sizes, across all Kelvin and MRG radar volumes (radius=157 km, domain area \cong 76 752 km ²) in this study using a 15 dBZ reflectivity blob detection threshold on the 0-2 km altitude layer. Statistical significance is indicated as in Fig. 12. | 87 |
| 16 | Observed MCS rain area and corresponding MCS porosity fraction in this study, using a 15 dBZ reflectivity blob detection threshold on the 0-2 km altitude layer, for Kelvin radar volumes (dot) and MRG radar volumes (x), where radius=157 km and domain area \cong 76 752 km ² . Zero porosity indicates that the MCS had no interior areas with reflectivity < 15 dBZ. | 88 |

| | | |
|----|--|----|
| 17 | CFADs of reflectivity for our Kelvin trough radar volumes (a,b,c) and MRG trough volumes (d,e,f) for total precipitation areas (a,d) as well as precipitation categorized as convective (b,e) and stratiform (c,f). Contours are plotted at 0.125% data $\text{dBZ}^{-1}\text{km}^{-1}$. Vertical lines are drawn on (a,b,c) to approximate the near-surface modal ensemble total, convective, and stratiform reflectivities for the Kelvin data, and the lines are reproduced in the same place for MRG data. | 89 |
| 18 | As in Fig. 17, but using S06 wave event data. | 90 |
| 19 | (Yuter and Houze 1995 Fig. 8a) CFAD of radar reflectivity from a stratiform region observed to the rear of a Kansas squall line at 0345 UTC 11 June 1985 during the PRE-STORM project. Bin size is 2.5 dBZ, contoured at 5% $\text{dBZ}^{-1}\text{km}^{-1}$ intervals. | 91 |
| 20 | Schematic representation, with a radar reflectivity plan view and vertical cross section, of (a) an idealized mature-stage leading-line trailing-stratiform MCS (based on Fig. 1c of Leary and Houze 1979), and (b) an MCS more typical of Kwajalein and the west Pacific warm pool. The outside contour represents the weakest detectable radar reflectivity, and successive inner contours and shadings represent successively stronger reflectivities. Dark arrows represent hydrometeor particle trajectories emanating from the convective region(s). | 92 |
| 21 | Normalized frequency distributions of vertical wind shear in the 1000-700 hPa layer in this study. Shear speed and direction for (a) all 1999-2003 rainy season soundings; (b) all 59 Kelvin and 33 MRG soundings; (c) the 23 Kelvin and 6 MRG soundings that are closest in time to when convective lines were at maximum visible organization during Kelvin and MRG events. | 93 |

- 22 (Fig. 4 from Johnson et al. 2005) Schematic depiction from LeMone et al. (1998) of four main categories of convective structures for given low-level (1000-800 hPa) and mid-level (800-400 hPa) vertical wind shears based on TOGA COARE observations and modified to include results from SCSMEX (Johnson et al. 2005). Specifically, modes 2r and 4c were added. Lengths of the convective bands are 100 to 300 km; line segments in upper-left panel are up to 50 km long. The cutoff between ‘strong’ and ‘weak’ shear for the low-levels is 4 ms^{-1} and for mid-levels is 5 ms^{-1} . Arrows marked L and M are shear vectors for low- and mid-levels, respectively. 94
- 23 Observed stratiform rain area per total rain area across all Kelvin and MRG radar volumes in (a) our trough dataset and in (b) the S06 wave dataset. Total area and stratiform area fraction are calculated on the 0-2 km altitude layer of radar volumes (radius=157 km, domain area \cong 76 752 km²). 95
- 24 Observed stratiform rain area fractions per total rain area across all Kelvin and MRG radar volumes in this study. (a) is a scatter plot version, and to more clearly indicate the frequency distribution, (b) is a density plot representation of (a) with shadings representing fractional frequency. Stratiform area fraction is calculated on the 0-2 km altitude layer of radar volumes (radius=157 km, domain area \cong 76 752 km²). Stratiform fractions below 0.3 are infrequent and omitted. Note that there are no stratiform area fractions for MRG for total rain areas $> 46\,224 \text{ km}^2$ because such total areas were not observed for MRG cases. 96

25 As in 24, but with observed convective precipitation areas per total rain area. Convective rain areas $> 10\,716\text{ km}^2$ only occur in the Kelvin data. These large convective areas are reached and sustained during two Kelvin wave events. The maximum observed convective area is about 20% of the radar domain ($\sim 15\,500\text{ km}^2$). 97

26 (Wheeler et al. 2000 Fig. 7) Longitude-height cross sections along the equator of the vertical velocity (shading), temperature (contours), and zonal-vertical wind (vectors) anomalies associated with the OLR variation of the convectively-coupled Kelvin wave at the base point $0^\circ, 90^\circ\text{E}$, for day -3, day +1, and day +5. Lightest shading shows downward velocity $< -0.1\text{ cm s}^{-1}$, medium shading for upward velocity $> 0.1\text{ cm s}^{-1}$, and darkest shading for upward velocity $> 0.2\text{ cm s}^{-1}$. Contour interval for temperature is 0.1 K, with negative contours dashed. Vector vertical wind component is multiplied by a factor of 500, and the largest labeled vectors (top-right corner) are in units of meters per second. Single and double bars at the top of each plot show the positions of the OLR anomalies $< -5\text{ W m}^{-2}$ and $> 5\text{ W m}^{-2}$, respectively. Wind vectors are locally statistically significant at the 99% level, and the contours are only shown within two levels vertically or 15° horizontally of points that are locally significant at the 99% level. 98

- 27 (Wheeler et al. 2000 Fig. 15) As in Fig. 26 except for the convectively-coupled mixed Rossby-gravity wave at the base point 7.5°N , 177.5°E , shown along 7.5°N . The times are for the lags of day -2.5, day 0, and day +5. Shading, contours, and vectors are as in Fig. 26. The thick single and double bars at the top of each plot show the positions of the OLR anomalies $<-5 \text{ W m}^{-2}$ and $>5 \text{ W m}^{-2}$, respectively. 99
- 28 Density plots of the normalized frequency distribution of effective echo heights for Kelvin (a,b) and MRG (c,d) convective (a,c) and stratiform (b,d) precipitation areas. Shadings represent fractional frequency, and the same shading scale is used in each plot. Altitude bins are centered on each 2 km layer of radar data (for example, the 1 km bin represents the 0-2 km altitude layer). 100

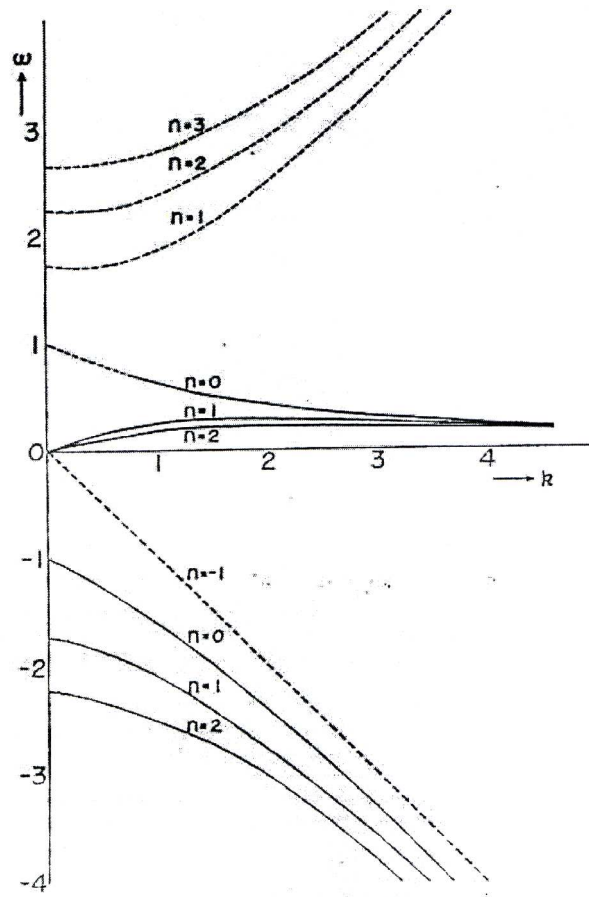


FIG. 1. (Matsuno 1966 Fig. 3a) Frequencies as functions of wave number. Thin solid line: eastward propagating inertio-gravity waves. Thin dashed line: westward propagating inertio-gravity waves. Thick dashed line: Wave that is like the Kelvin wave.

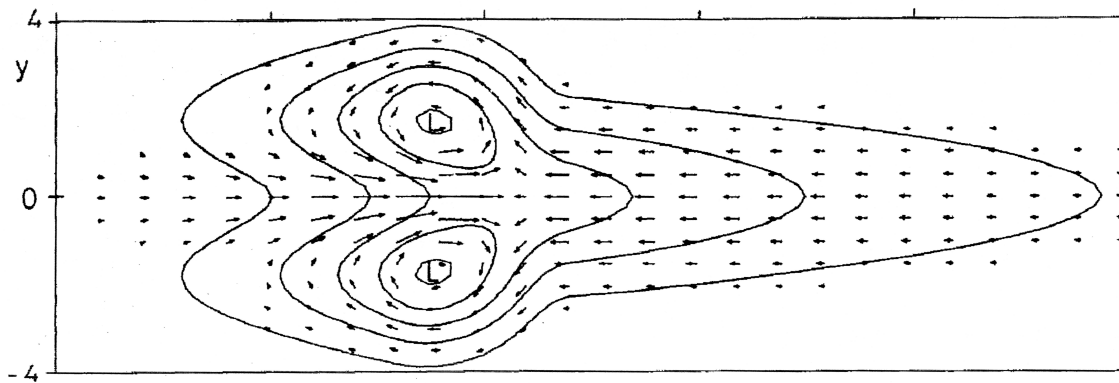


FIG. 2. (Gill 1980 Fig. 1b) Linear model solution for a heating region symmetric about the equator. The heating source exists at the convergence line just east of the two cyclones. Contours of perturbation pressure are shown (contoured every 0.3), which is negative everywhere. Arrows indicate the velocity field for the lower layer of the model. The Kelvin wave emanates eastward from the heating source, with associated easterly winds, while a planetary wave emanates westward with associated westerlies.

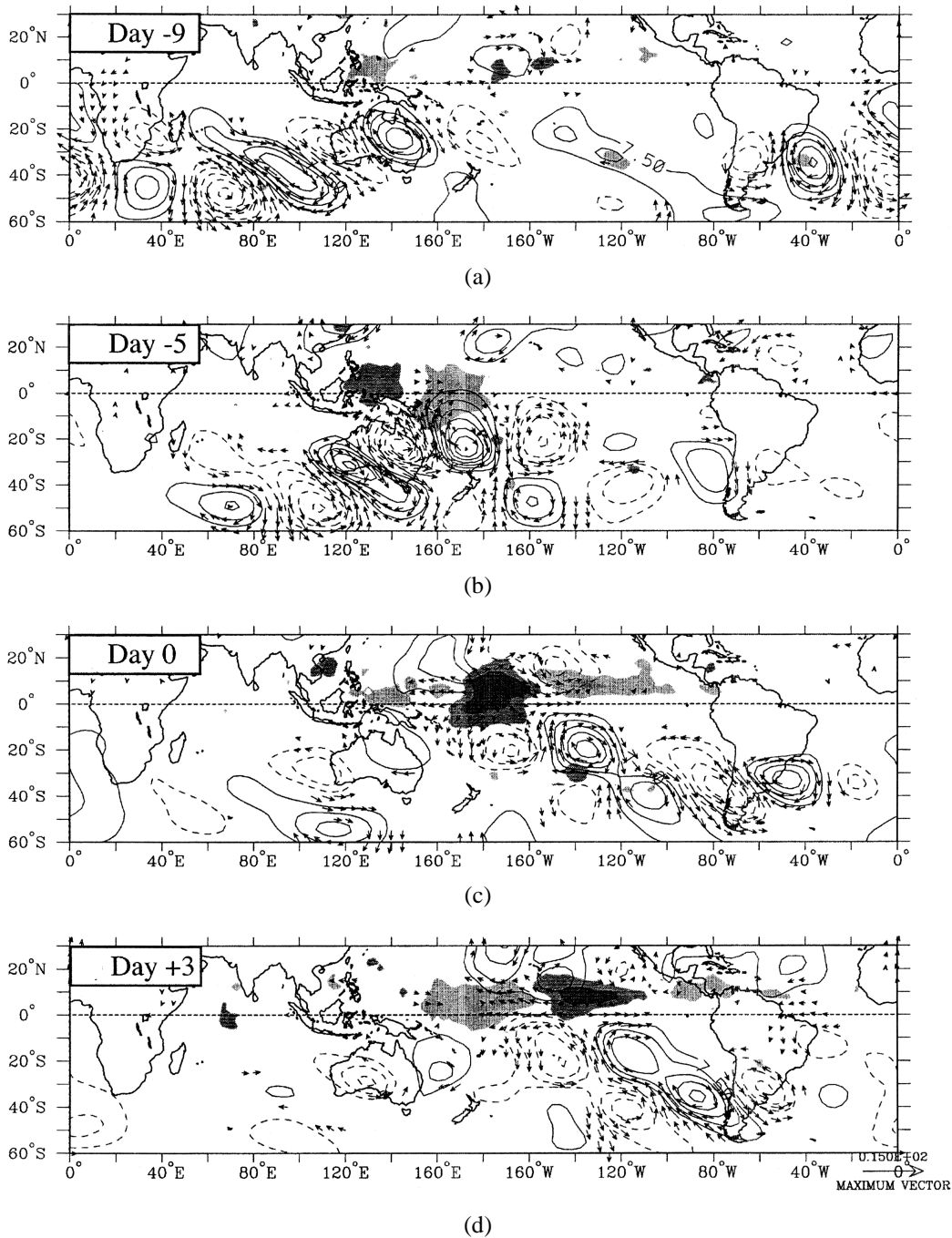
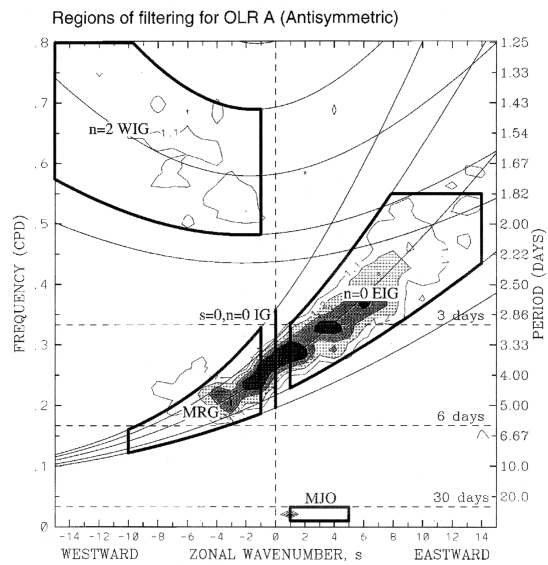
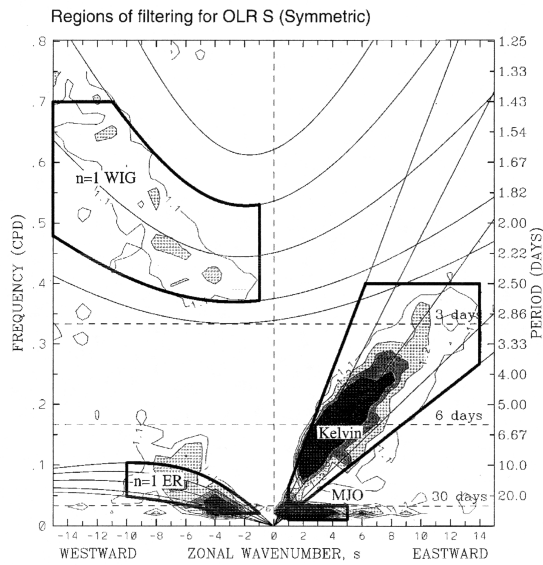


FIG. 3. (Straub and Kiladis 2003a Fig. 2) Regressed OLR (shading), 200 hPa streamfunction (contours), and winds (vectors) at lag times noted. These values are based on a -40 Wm^{-2} anomaly in Kelvin wave-filtered OLR at 7.5°N 172.5°W for the 15 Southern Hemisphere winters 1979-1993. OLR shading is at ± 6 and 15 Wm^{-2} (dark shading is negative), streamfunction contours are every $7.5 \times 10^5 \text{ m}^2 \text{ s}^{-1}$ (zero contour omitted), and the longest wind vectors correspond to a 10 ms^{-1} wind (only u and v values significant to at least 95% are shown; significance is determined using a local two-sided test to account for correlation and degrees of freedom).

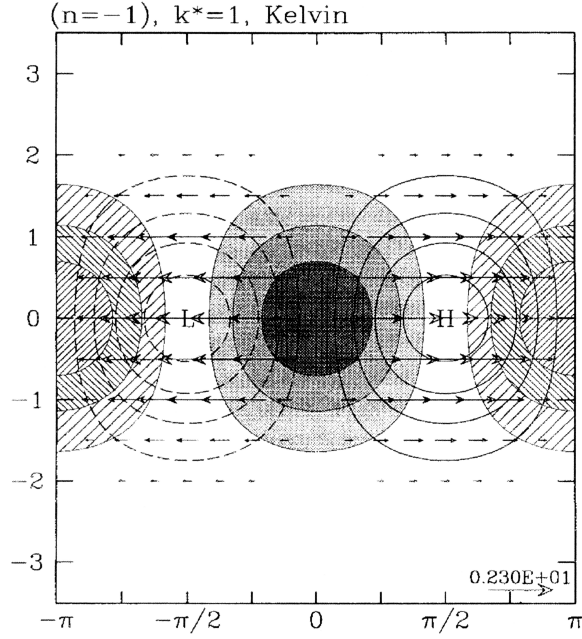


(a)

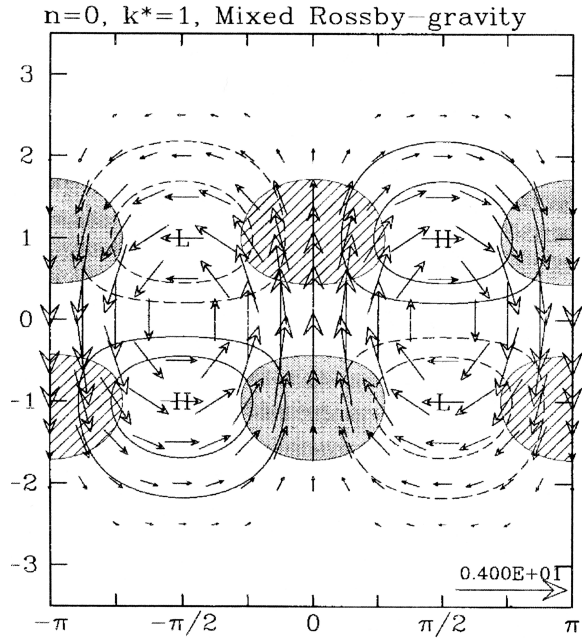


(b)

FIG. 4. (Wheeler and Kiladis 1999 Fig. 6) The (a) antisymmetric and (b) symmetric OLR power spectra (across January 1979-August 1996, summed across $10^{\circ}\text{S} - 10^{\circ}\text{N}$, with base-10 logarithm taken) divided by the background power spectra (arrived at by averaging the individual power spectra and smoothing wavenumber and frequency). Contours less than 1.1 or greater than 1.4 are omitted. Thin lines are the various equatorial wave dispersion curves for the different equivalent depths ($h=8, 12, 25, 50, 90$ m). Thick boxes indicate the regions of the wavenumber-frequency domain that are used to filter OLR data for specific wave types.

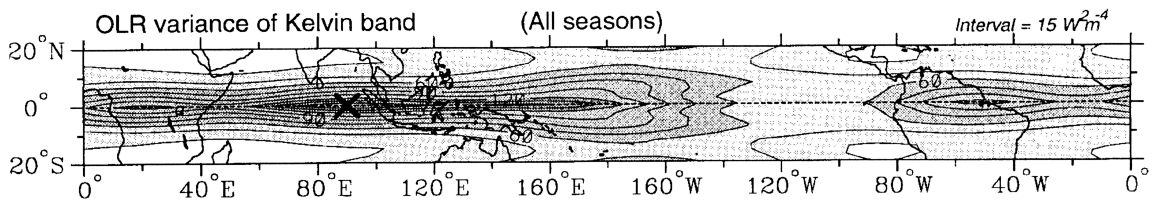


(a)

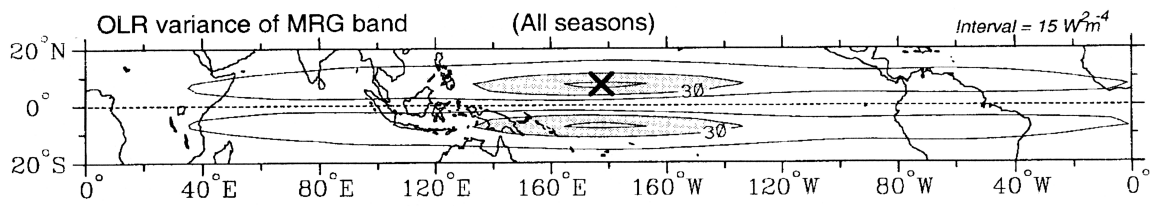


(b)

FIG. 5. (Wheeler et al. 2000 (a) Figure 6 (b) Figure 14) The theoretical equatorially trapped (a) Kelvin wave solution and (b) MRG wave solution to the linear shallow water equations on an equatorial β -plane (as in Matsuno 1966) for zonal wavenumber 1. Hatching indicates convergence and shading indicates divergence at a 0.6 interval. Unshaded contours are geopotential at a 0.5 interval. Negative contours are dashed and the zero contour is omitted. Vectors indicate wind, and the longest arrow is 2.3 units. Dimensional scales are as in Matsuno (1966).



(a)



(b)

FIG. 6. (Wheeler et al. 2000 Fig. 3a and Fig. 3e). Geographical distribution of (a) Kelvin-filtered OLR variance and (b) MRG-filtered OLR variance for all seasons across January 1979-August 1996. Contour interval is $15 (\text{Wm}^{-2})^2$. A thick X marks the point of maximum variance – in the eastern Indian Ocean for Kelvin, in the west-central Pacific Ocean for MRG.

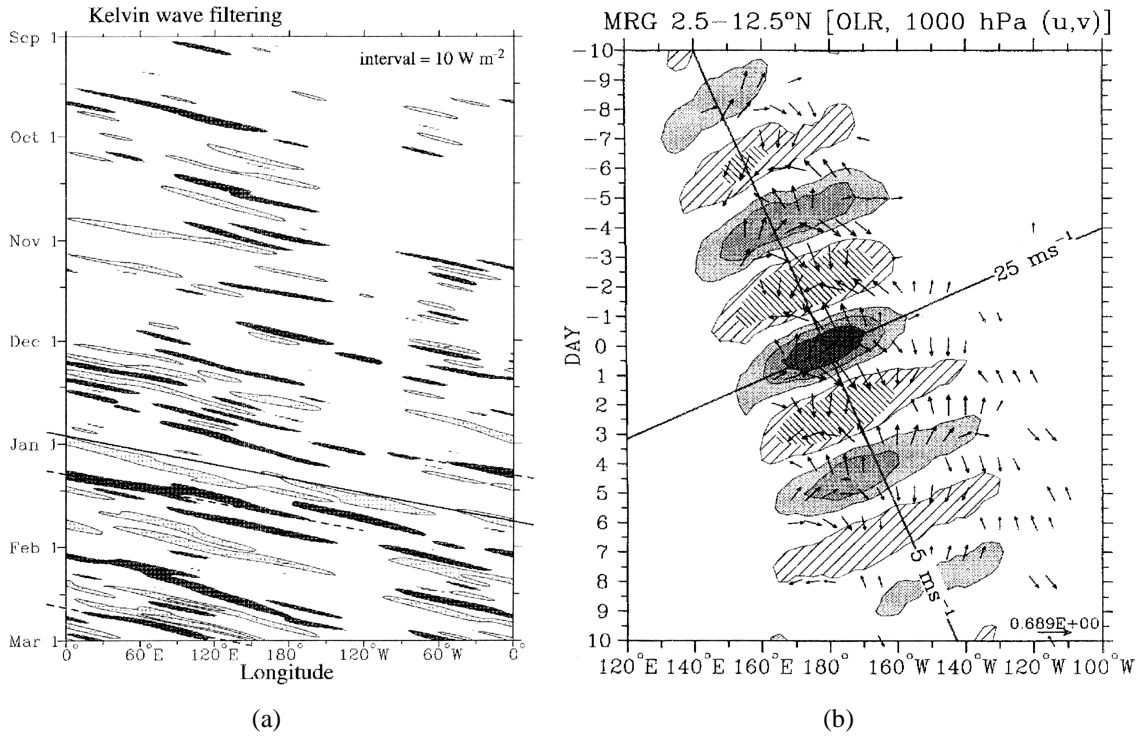


FIG. 7. ((a)Wheeler and Kiladis 1999 Fig. 9b, (b) Wheeler et al. 2000 Fig. 12) (a) Time-longitude section of the OLR anomalies for the Kelvin wave-filtered band for 0600 UTC 1 September 1992 - 0600 UTC 1 March 1993 averaged across 10°S - 2.5°N . Solid and dashed lines correspond to convectively coupled Kelvin wave disturbances. (b) Time-longitude diagram of anomalies of OLR (hatching/shading) and 1000 hPa zonal-meridional wind (vector) associated with the OLR variation of the convectively coupled MRG wave at base point 7.5°N 177.5°E . Each field is averaged across $2.5 - 12.5^{\circ}\text{N}$. Two levels of hatching denote OLR anomalies greater than 4 and 8 W m^{-2} , and the three levels of shading denote OLR anomalies less than -4, -8, and -12 W m^{-2} , respectively. Wind vectors are locally significant to 99%, with the largest vector 0.69 ms^{-1} .

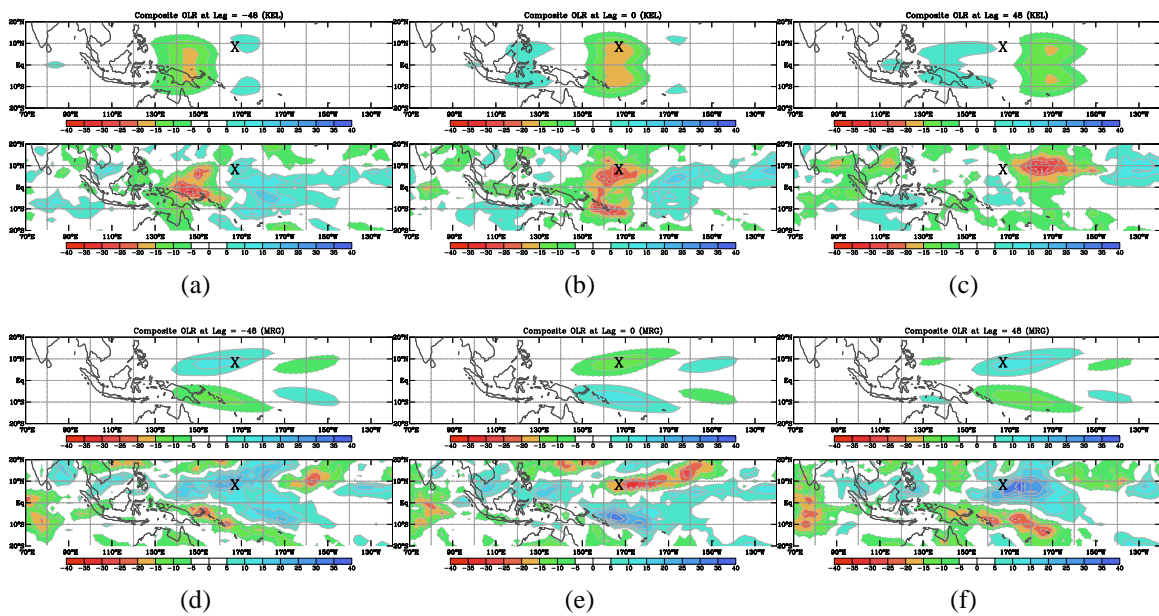


FIG. 8. Kelvin (a-c) and MRG (d-f) OLR anomaly data for this study. The top row of each wave type is the wave-filtered OLR anomaly data, and the bottom row is the raw OLR anomaly data. Lag times are given as -48 h (a,d), 0 h (b,e), and +48 h (c,f). An X marks the location of Kwajalein.

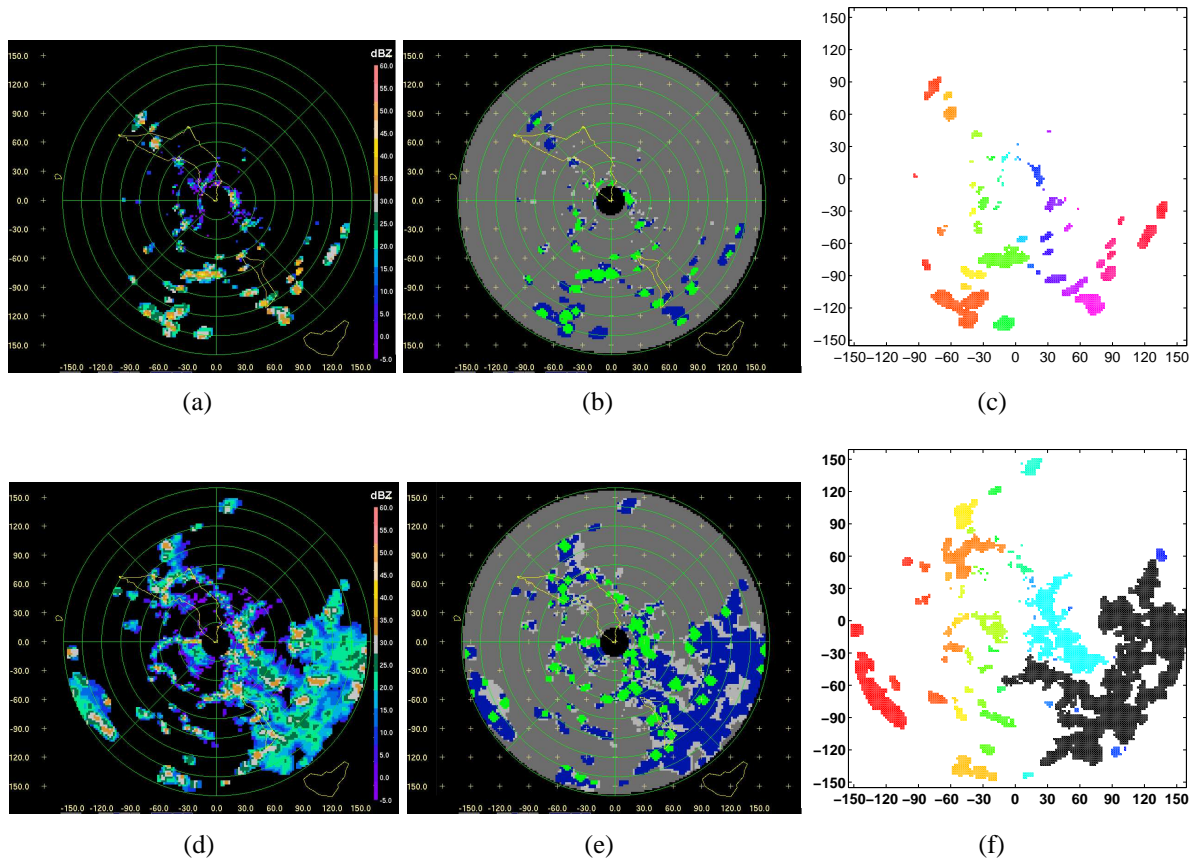


FIG. 9. Example reflectivity (a,d), convective-stratiform-weak (b,e, see Section 3), and blob detection (c,f, see Section 4) representations of two different organizational regimes in this study – isolated (a-c, 0549 UTC 13 December 2001), and large rain areas with embedded convection (coexistent with some isolated, d-f, 0223 UTC 30 October 1999). These images represent data from the 0-2 km altitude layers of the three-dimensional radar volumes (radius=157 km). Distance scales are in km. Convective-stratiform-weak map colors represent weak echo (light gray), stratiform echo (blue), and convective echo (green). Individual colors on the blob detection represent different individual contiguous rain blobs. The dark MCS blob in (f) is referred to in the text for its porosity, which is 0.089, totals 919 km², and is evident as white space within the blob.

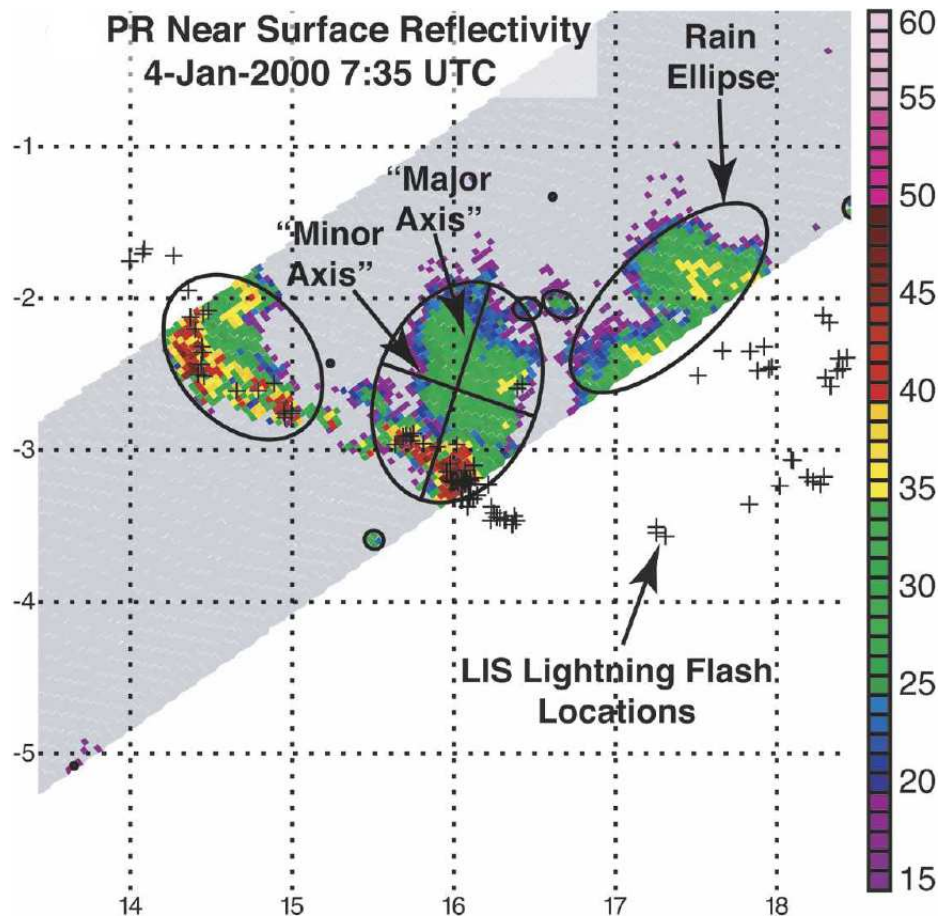
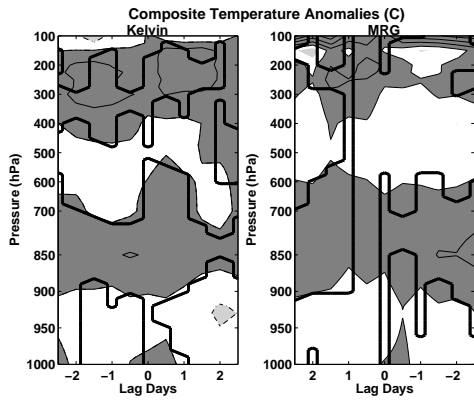
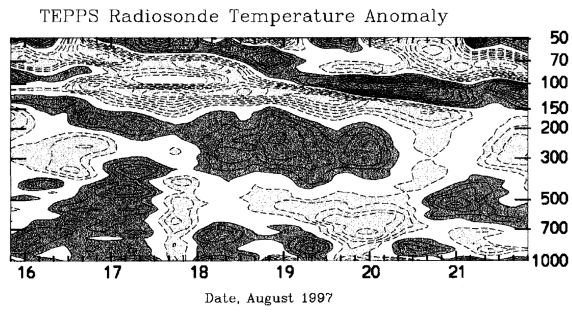


FIG. 10. (Nesbitt et al. 2006 Fig. 1d) TRMM PR near-surface reflectivity (shading, dBZ), TRMM Lightning Imaging Sensor lightning flashes (plus signs), and locations of best-fit ellipses of precipitation features within each scene. The major and minor axes are labeled for the largest precipitation feature.

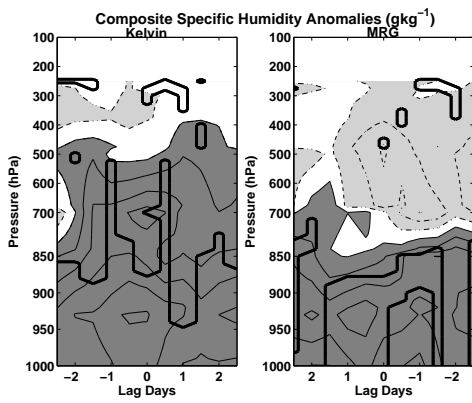
FIG. 11. Time-lag composite sounding anomalies for temperature (a,b), specific humidity (c,d), and zonal wind (e,f). Kelvin and MRG composites for this study (a,c,e) are in 12 h intervals, temporally smoothed for display using a 36 h running mean. Soundings during a TEPPS Kelvin wave event (b,d,f) correspond to Straub and Kiladis (2002) Figs. 10, 14, and 11, respectively, with 4 h resolution. Darker shading and solid contours represent positive values. Contour intervals are: (a) 0.25 °C, no values $<|0.25|$; (b) 0.3 °C, no zero values; (c) 0.125 gkg⁻¹, no values $<|0.125|$; (d) 0.3 gkg⁻¹, no zero values; (e) 0.375 ms⁻¹, no values $<|0.375|$; (f) 1.0 ms⁻¹, no zero values. Areas in (a,c,e) significantly different to 90% (Student's t-test) from the full July-December 1999-2003 dataset are outlined in bold contour. Time scales in (a,c,e) reflect one full ridge-trough-ridge wavelength. The MRG time axis has been reversed because MRG waves move east to west.



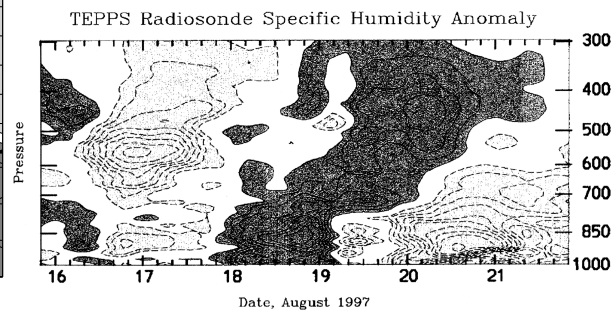
(a)



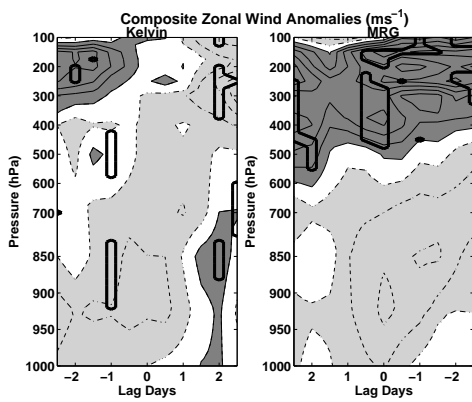
(b)



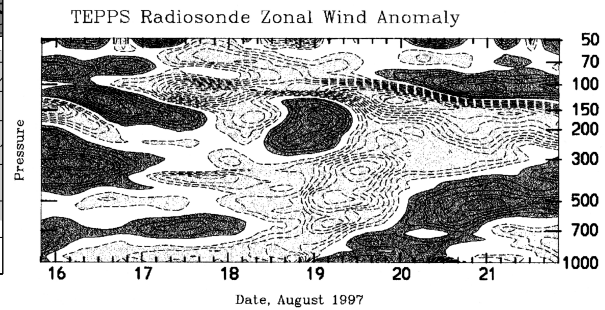
(c)



(d)



(e)



(f)

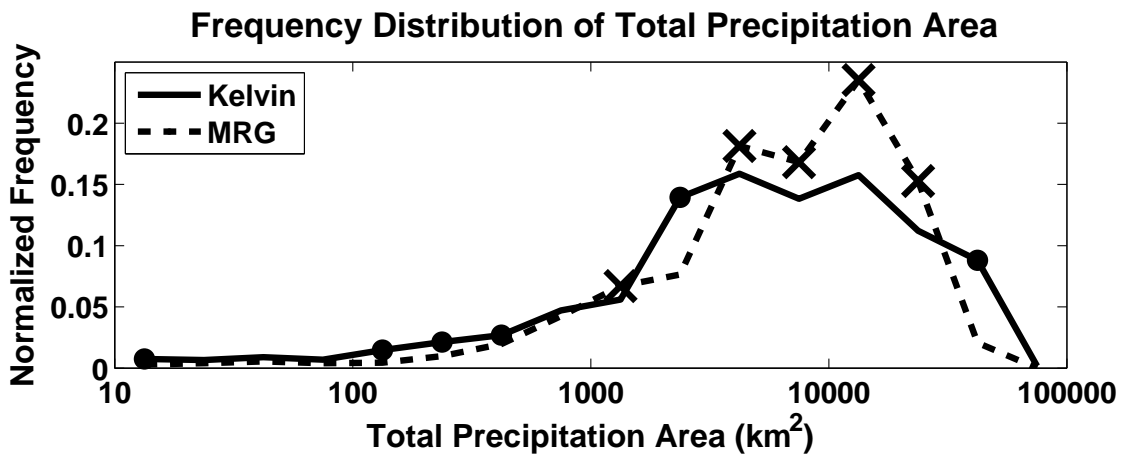
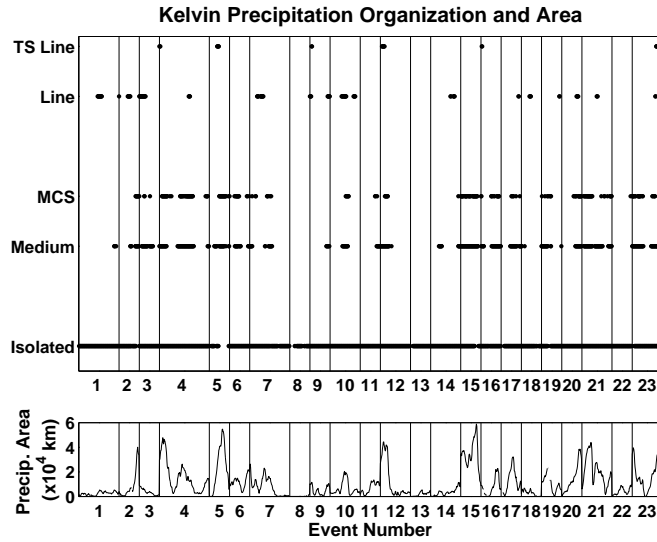
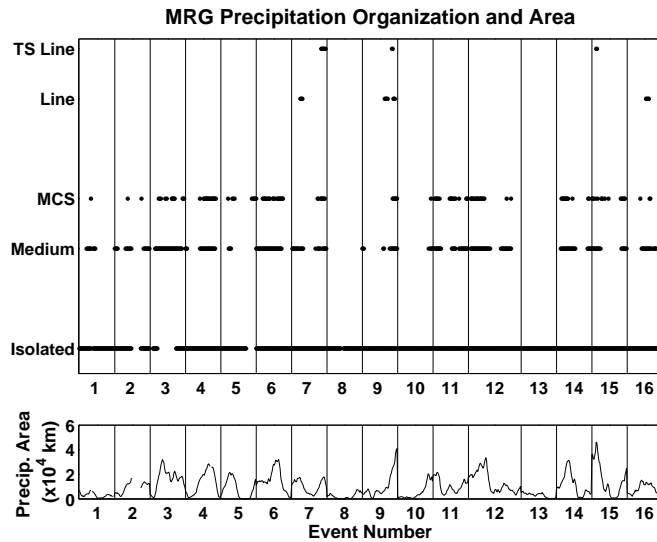


FIG. 12. Normalized frequency of occurrence of total rain areas across all Kelvin and MRG radar volumes using a reflectivity threshold of 15 dBZ on the 0-2 km altitude layer of radar volumes (radius=157 km, domain area \cong 76 752 km²) and plotted on a logarithmic scale. Dots are placed where Kelvin data have a significantly higher frequency of that particular rain area bin than MRG, and likewise an X is placed along the MRG line where MRG has a significantly higher frequency than Kelvin. Significance is calculated to 95% using a 10 000-member Monte Carlo test.



(a)



(b)

FIG. 13. Horizontal precipitation organization for (a) Kelvin radar volumes and (b) MRG volumes in this study, along with observed precipitation areas (bottom of each). Organization is determined visually (Section 3) using half-hour intervals of the 0-2 km altitude layer of radar volumes (radius=157 km, domain area $\cong 76\,752\text{ km}^2$); precipitation areas are also extracted at these half-hour intervals. Wave events are bounded by vertical lines, and a point is placed at each time for the type(s) of organization seen at that time. Note that these are not continuous time series.

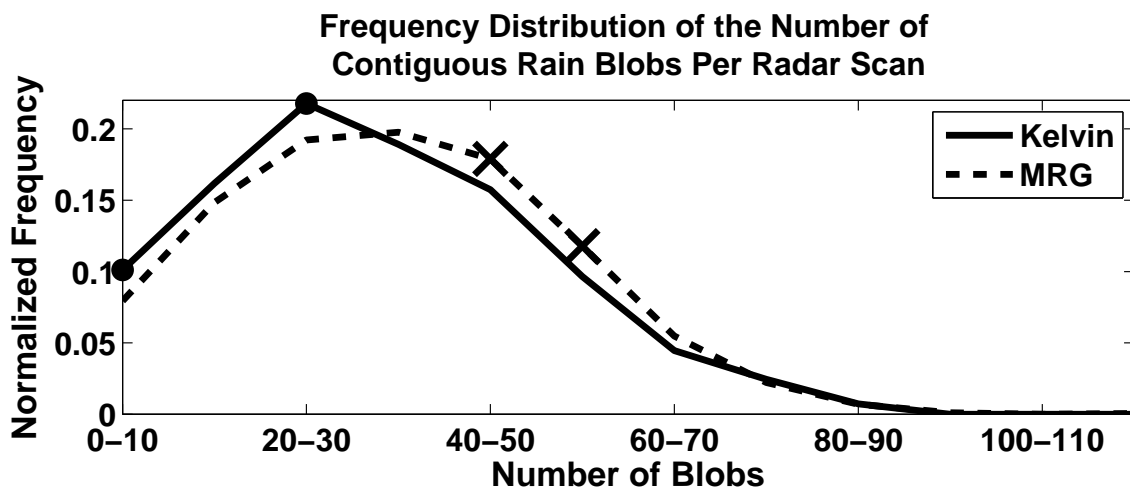


FIG. 14. Normalized frequency of occurrence of the number of blobs per radar scan (at the 0-2 km altitude layer of radar volumes, radius=157 km) across all Kelvin and MRG radar volumes using a blob reflectivity threshold of 15 dBZ. Statistical significance is indicated as in Fig. 12.

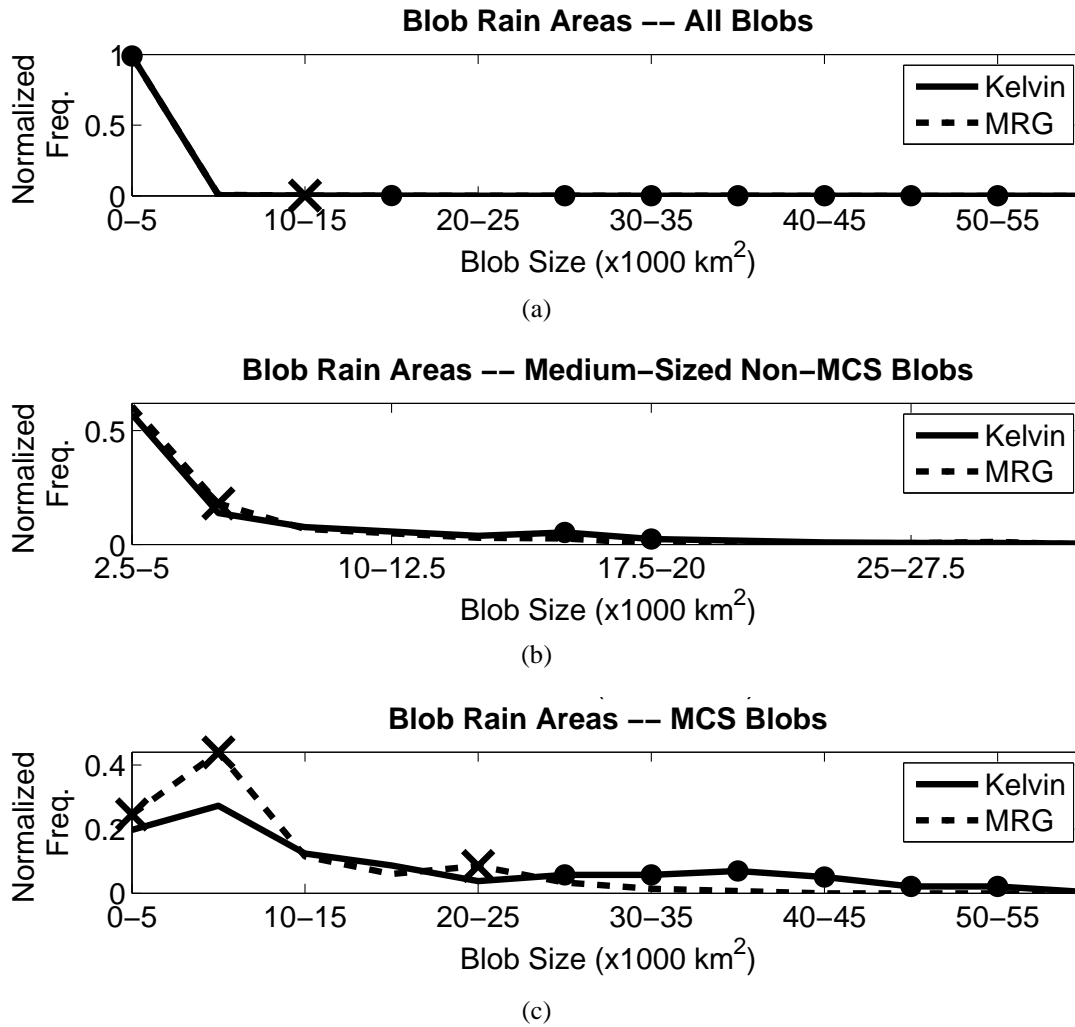


FIG. 15. Normalized frequency of occurrence of (a) all blob sizes, (b) ‘medium-sized’ non-MCS blobs, and (c) MCS blob sizes, across all Kelvin and MRG radar volumes (radius=157 km, domain area \cong 76 752 km²) in this study using a 15 dBZ reflectivity blob detection threshold on the 0-2 km altitude layer. Statistical significance is indicated as in Fig. 12.

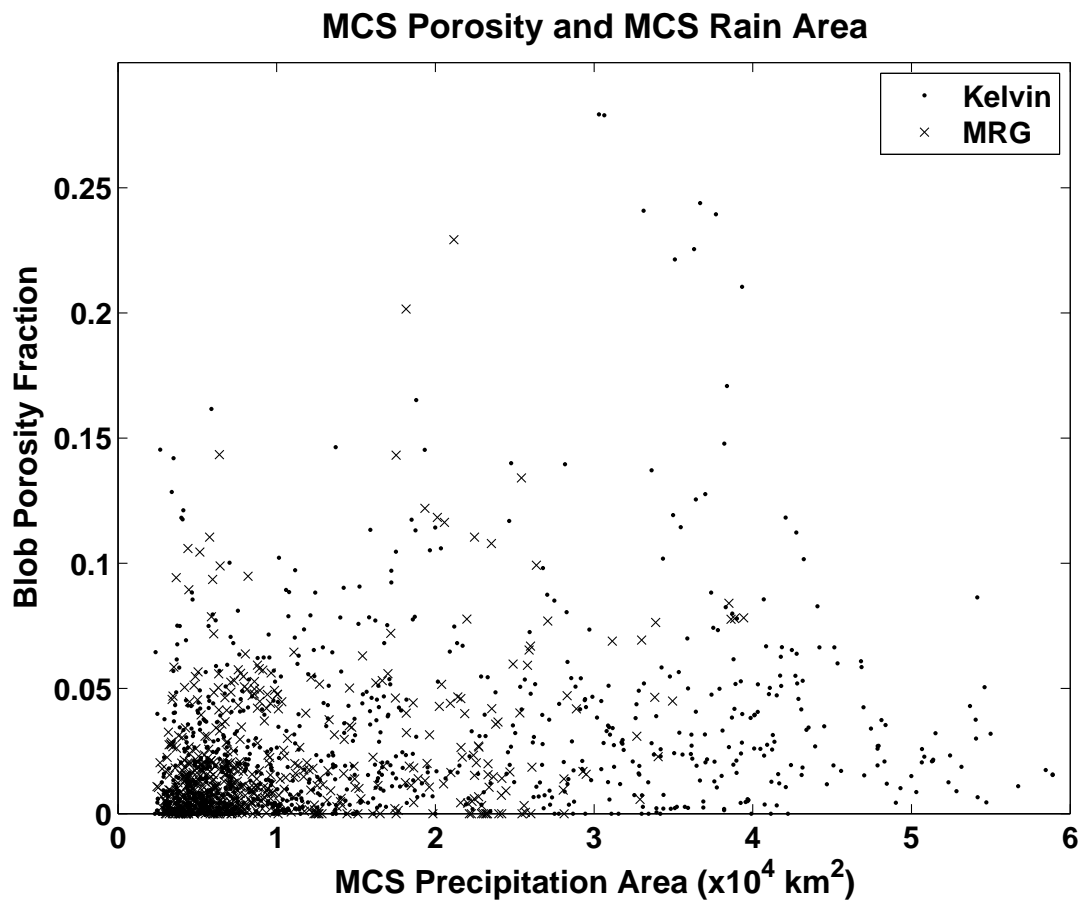


FIG. 16. Observed MCS rain area and corresponding MCS porosity fraction in this study, using a 15 dBZ reflectivity blob detection threshold on the 0-2 km altitude layer, for Kelvin radar volumes (dot) and MRG radar volumes (x), where radius=157 km and domain area \cong 76 752 km². Zero porosity indicates that the MCS had no interior areas with reflectivity < 15 dBZ.

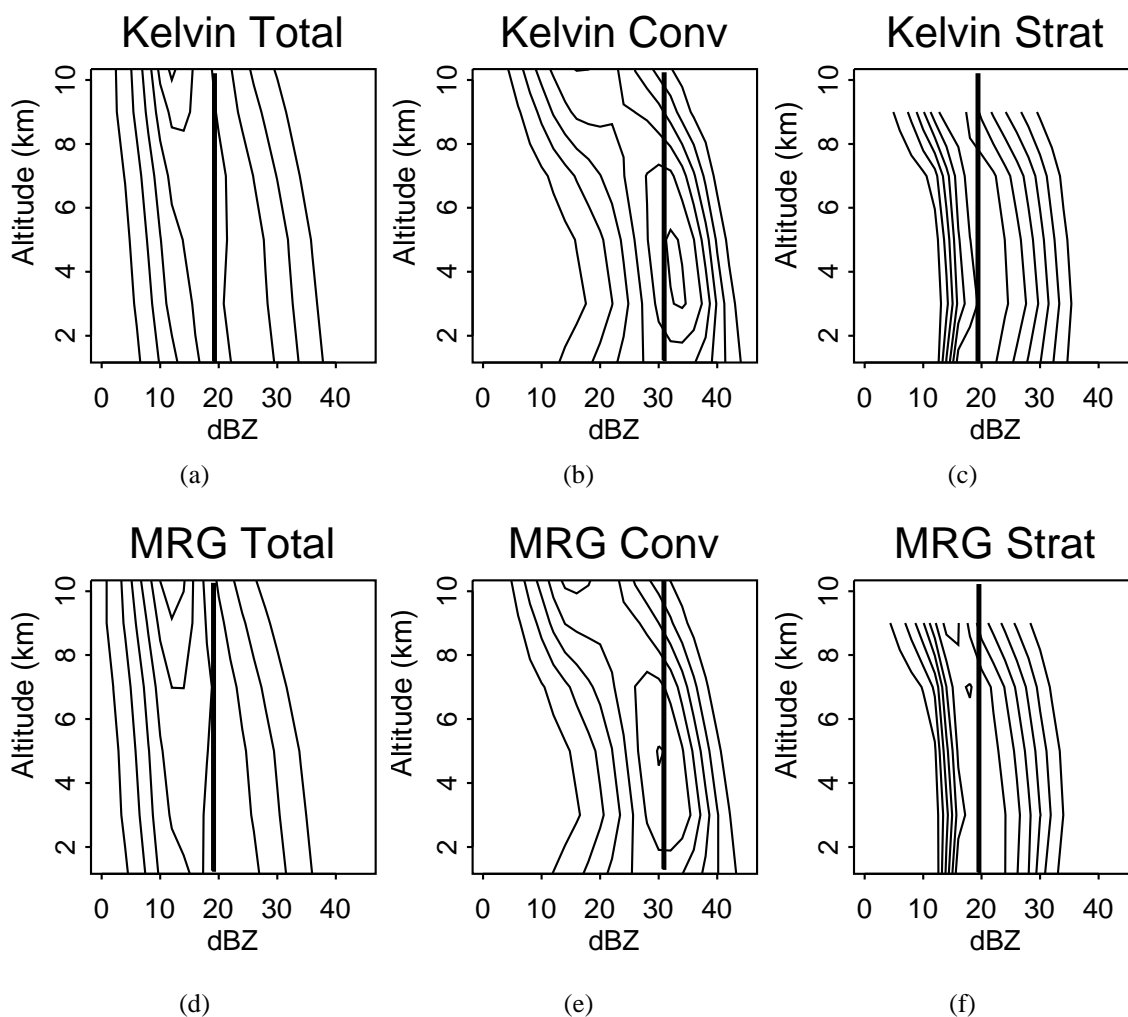


FIG. 17. CFADs of reflectivity for our Kelvin trough radar volumes (a,b,c) and MRG trough volumes (d,e,f) for total precipitation areas (a,d) as well as precipitation categorized as convective (b,e) and stratiform (c,f). Contours are plotted at $0.125\% \text{ data dBZ}^{-1}\text{km}^{-1}$. Vertical lines are drawn on (a,b,c) to approximate the near-surface modal ensemble total, convective, and stratiform reflectivities for the Kelvin data, and the lines are reproduced in the same place for MRG data.

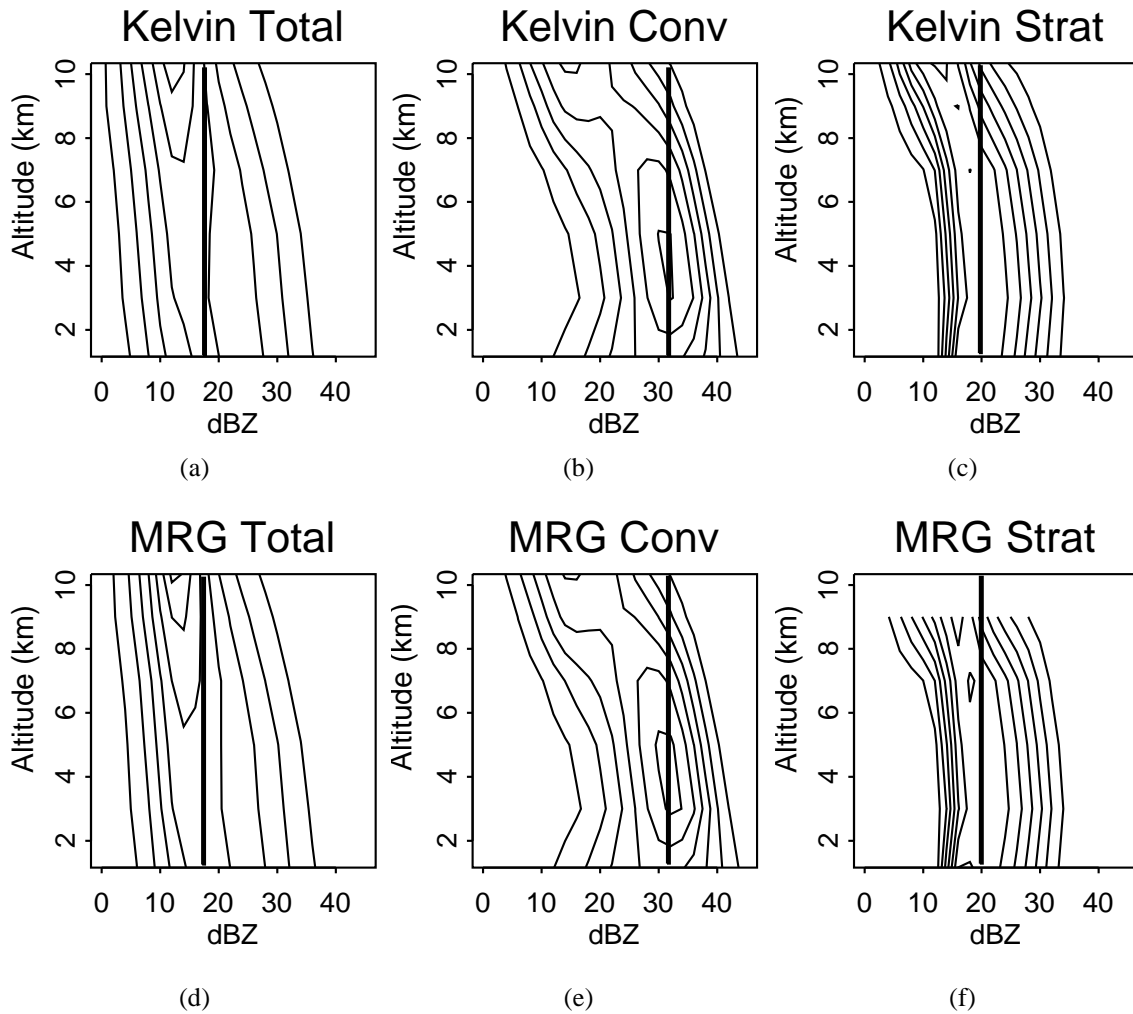


FIG. 18. As in Fig. 17, but using S06 wave event data.

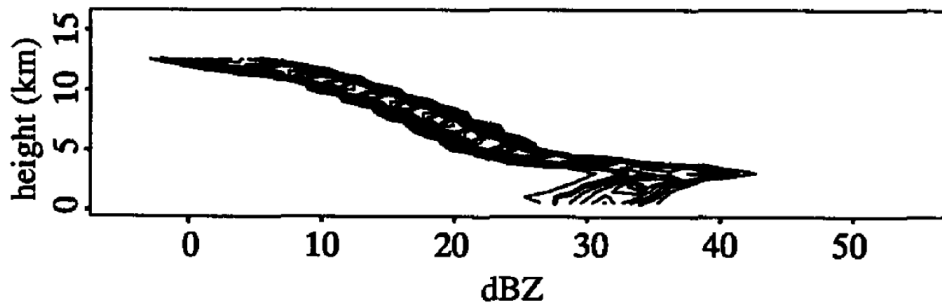
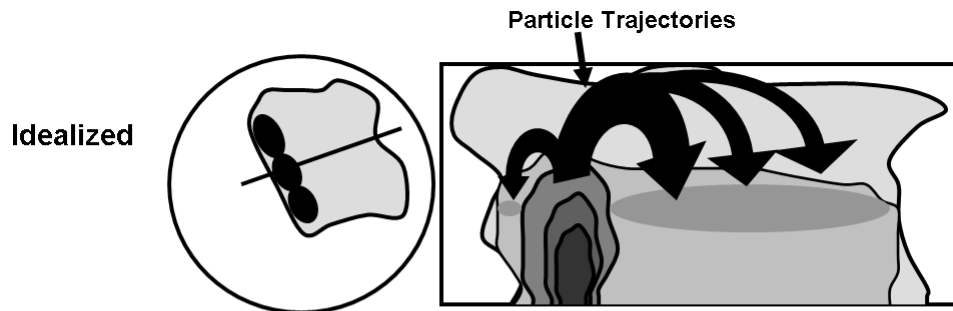
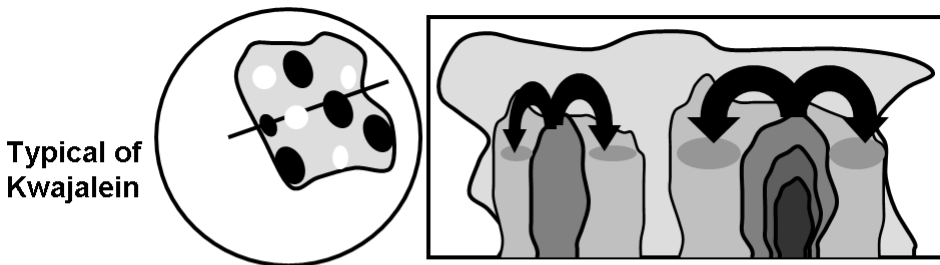


FIG. 19. (Yuter and Houze 1995 Fig. 8a) CFAD of radar reflectivity from a stratiform region observed to the rear of a Kansas squall line at 0345 UTC 11 June 1985 during the PRE-STORM project. Bin size is 2.5 dBZ, contoured at 5% $\text{dBZ}^{-1} \text{ km}^{-1}$ intervals.



(a)



(b)

FIG. 20. Schematic representation, with a radar reflectivity plan view and vertical cross section, of (a) an idealized mature-stage leading-line trailing-stratiform MCS (based on Fig. 1c of Leary and Houze 1979), and (b) an MCS more typical of Kwajalein and the west Pacific warm pool. The outside contour represents the weakest detectable radar reflectivity, and successive inner contours and shadings represent successively stronger reflectivities. Dark arrows represent hydrometeor particle trajectories emanating from the convective region(s).

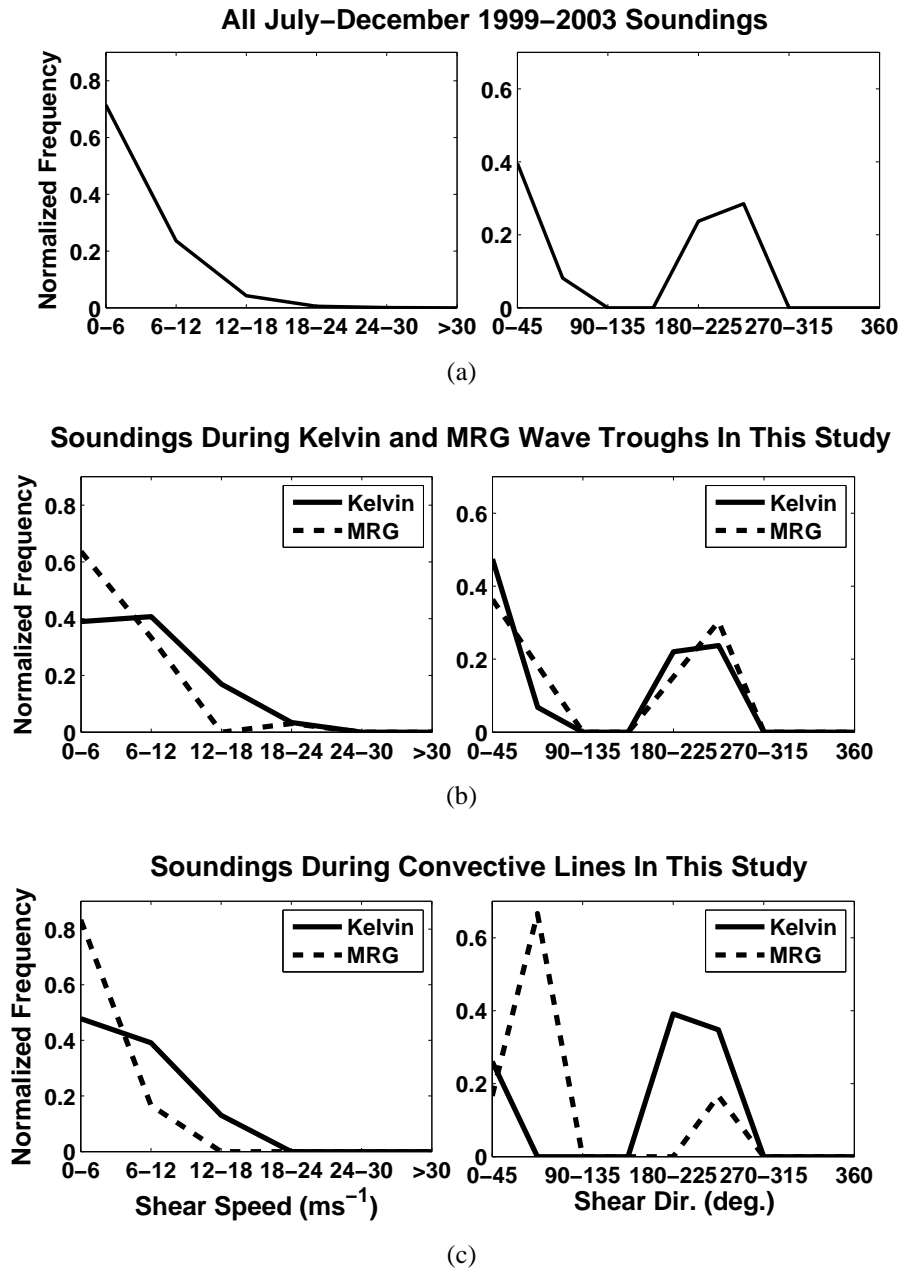


FIG. 21. Normalized frequency distributions of vertical wind shear in the 1000-700 hPa layer in this study. Shear speed and direction for (a) all 1999-2003 rainy season soundings; (b) all 59 Kelvin and 33 MRG soundings; (c) the 23 Kelvin and 6 MRG soundings that are closest in time to when convective lines were at maximum visible organization during Kelvin and MRG events.

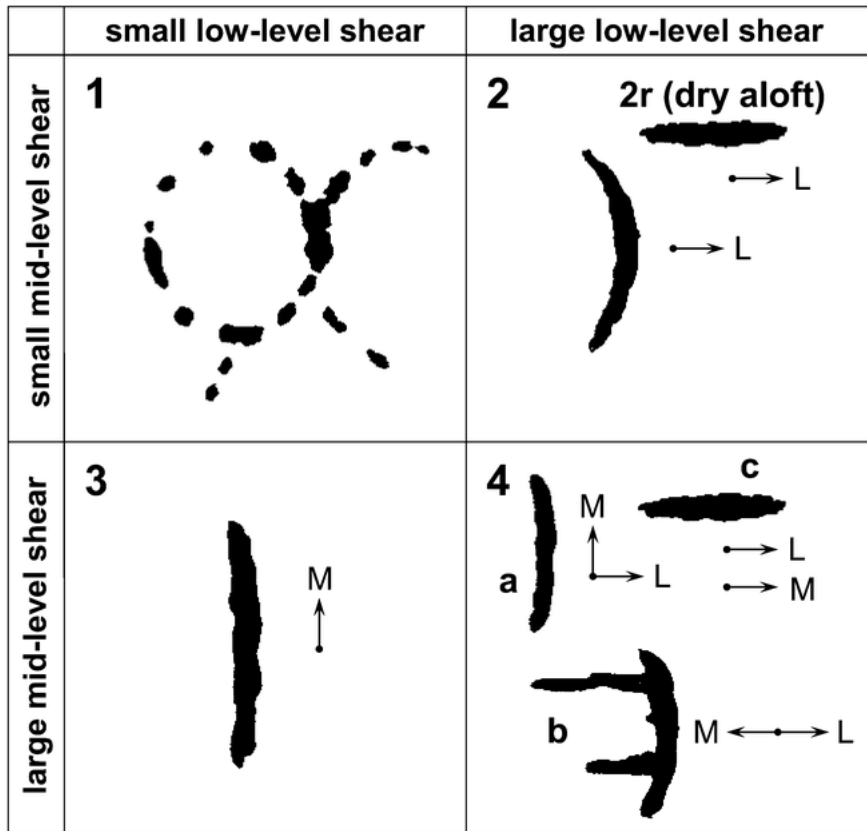


FIG. 22. (Fig. 4 from Johnson et al. 2005) Schematic depiction from LeMone et al. (1998) of four main categories of convective structures for given low-level (1000-800 hPa) and mid-level (800-400 hPa) vertical wind shears based on TOGA COARE observations and modified to include results from SCSMEX (Johnson et al. 2005). Specifically, modes 2r and 4c were added. Lengths of the convective bands are 100 to 300 km; line segments in upper-left panel are up to 50 km long. The cutoff between 'strong' and 'weak' shear for the low-levels is 4 ms^{-1} and for mid-levels is 5 ms^{-1} . Arrows marked L and M are shear vectors for low- and mid-levels, respectively.

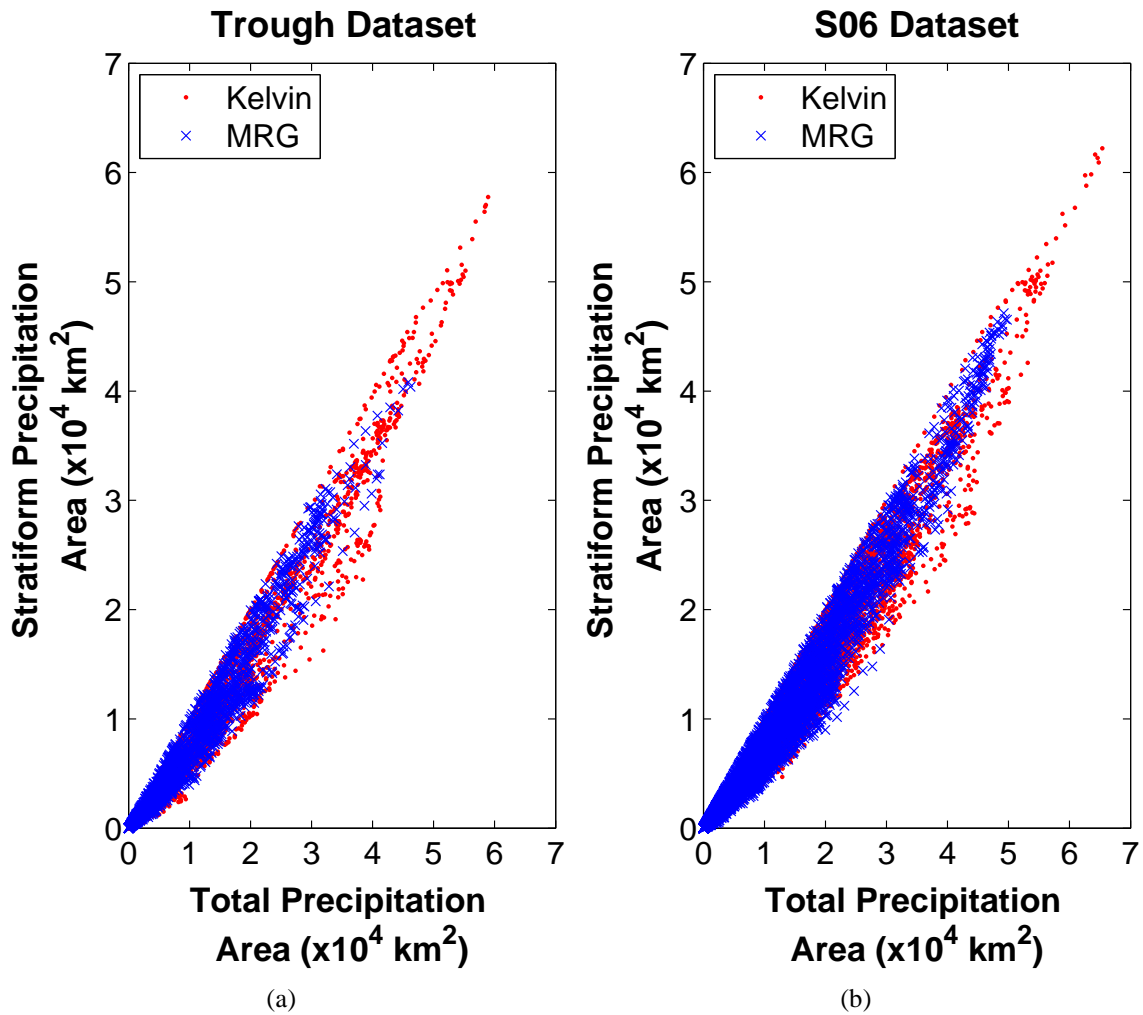
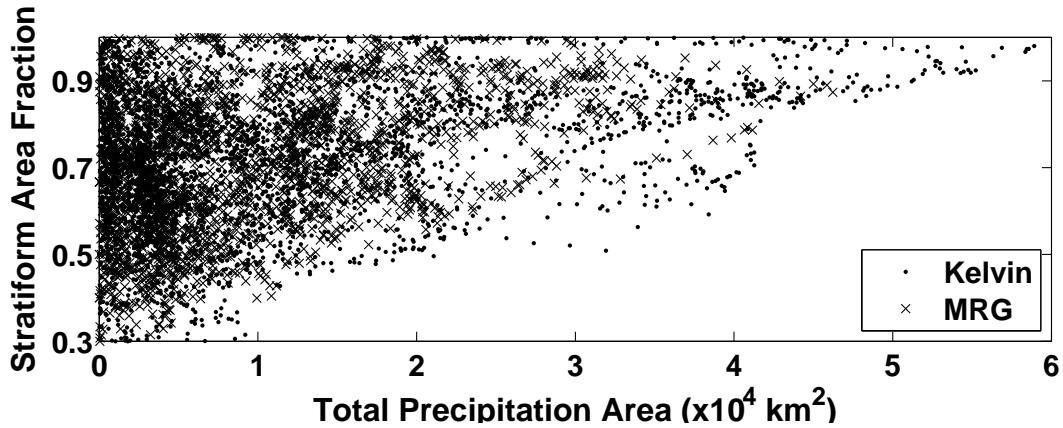
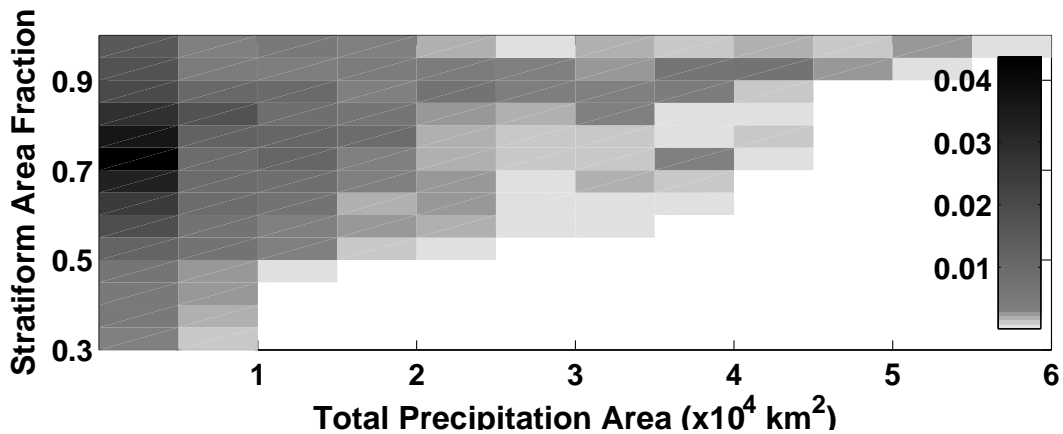


FIG. 23. Observed stratiform rain area per total rain area across all Kelvin and MRG radar volumes in (a) our trough dataset and in (b) the S06 wave dataset. Total area and stratiform area fraction are calculated on the 0-2 km altitude layer of radar volumes (radius=157 km, domain area \cong 76 752 km²).

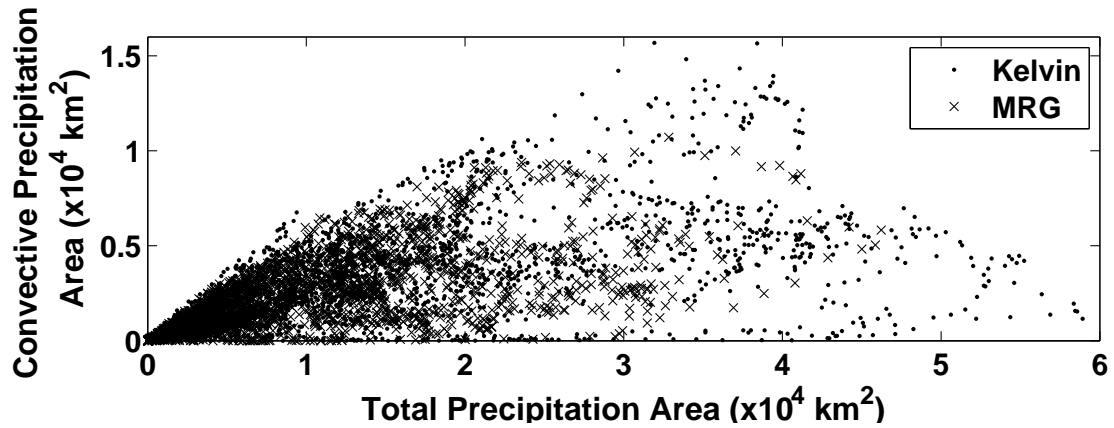


(a)

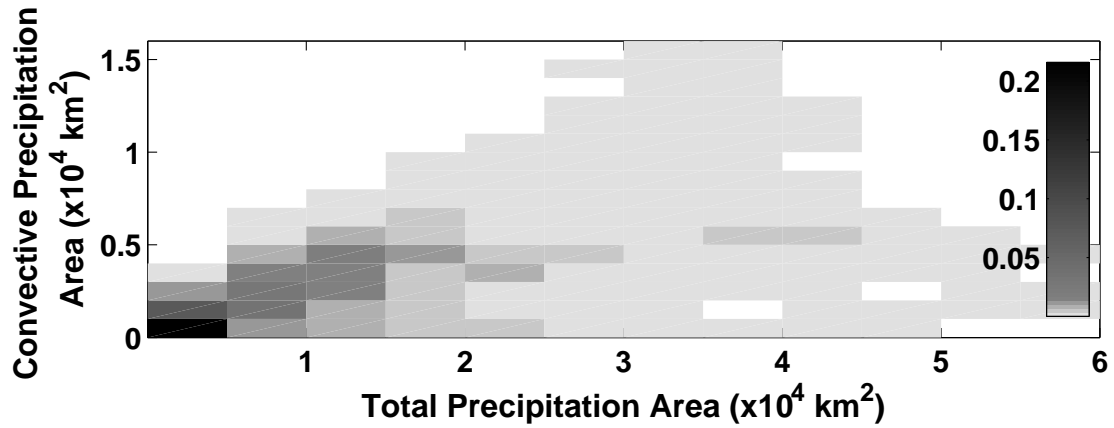


(b)

FIG. 24. Observed stratiform rain area fractions per total rain area across all Kelvin and MRG radar volumes in this study. (a) is a scatter plot version, and to more clearly indicate the frequency distribution, (b) is a density plot representation of (a) with shadings representing fractional frequency. Stratiform area fraction is calculated on the 0-2 km altitude layer of radar volumes (radius=157 km, domain area \cong 76 752 km²). Stratiform fractions below 0.3 are infrequent and omitted. Note that there are no stratiform area fractions for MRG for total rain areas > 46 224 km² because such total areas were not observed for MRG cases.



(a)



(b)

FIG. 25. As in 24, but with observed convective precipitation areas per total rain area. Convective rain areas $> 10\,716\text{ km}^2$ only occur in the Kelvin data. These large convective areas are reached and sustained during two Kelvin wave events. The maximum observed convective area is about 20% of the radar domain ($\sim 15\,500\text{ km}^2$).

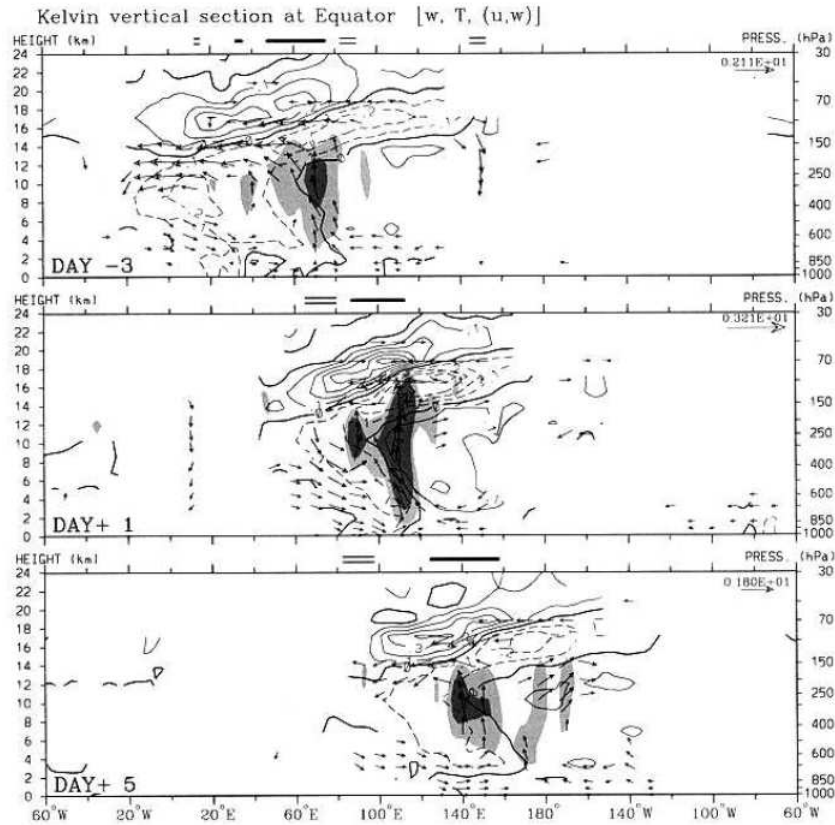


FIG. 26. (Wheeler et al. 2000 Fig. 7) Longitude-height cross sections along the equator of the vertical velocity (shading), temperature (contours), and zonal-vertical wind (vectors) anomalies associated with the OLR variation of the convectively-coupled Kelvin wave at the base point 0° , 90°E , for day -3, day +1, and day +5. Lightest shading shows downward velocity $< -0.1 \text{ cm s}^{-1}$, medium shading for upward velocity $> 0.1 \text{ cm s}^{-1}$, and darkest shading for upward velocity $> 0.2 \text{ cm s}^{-1}$. Contour interval for temperature is 0.1 K, with negative contours dashed. Vector vertical wind component is multiplied by a factor of 500, and the largest labeled vectors (top-right corner) are in units of meters per second. Single and double bars at the top of each plot show the positions of the OLR anomalies $< -5 \text{ W m}^{-2}$ and $> 5 \text{ W m}^{-2}$, respectively. Wind vectors are locally statistically significant at the 99% level, and the contours are only shown within two levels vertically or 15° horizontally of points that are locally significant at the 99% level.

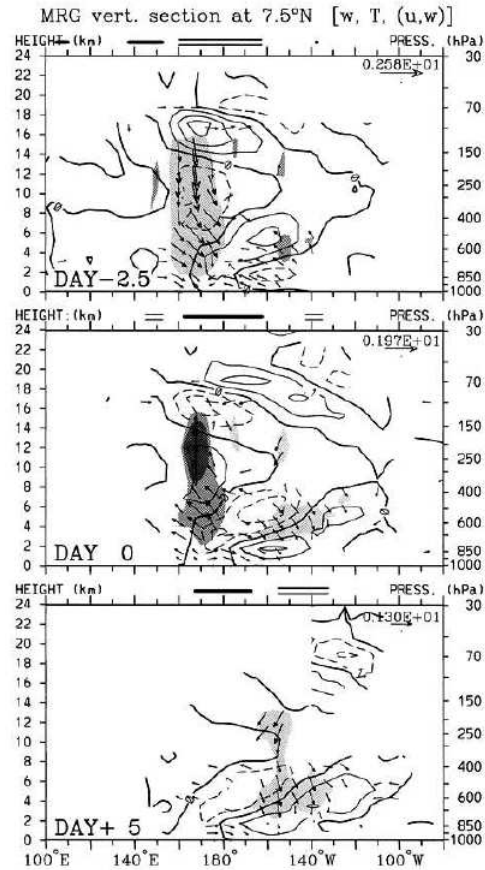


FIG. 27. (Wheeler et al. 2000 Fig. 15) As in Fig. 26 except for the convectively-coupled mixed Rossby-gravity wave at the base point 7.5 °N, 177.5 °E, shown along 7.5 °N. The times are for the lags of day -2.5, day 0, and day +5. Shading, contours, and vectors are as in Fig. 26. The thick single and double bars at the top of each plot show the positions of the OLR anomalies $<-5 \text{ W m}^{-2}$ and $>5 \text{ W m}^{-2}$, respectively.

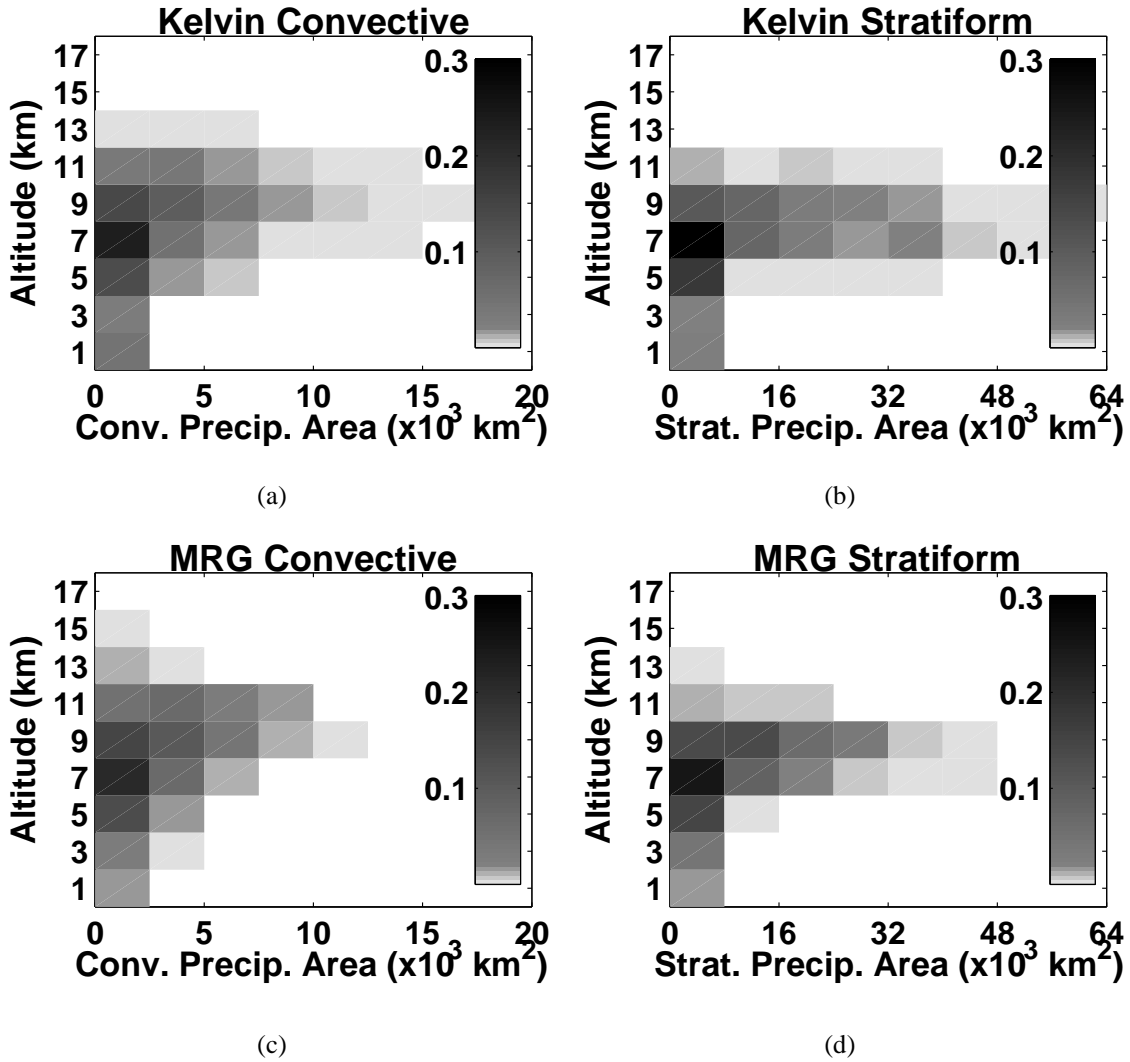


FIG. 28. Density plots of the normalized frequency distribution of effective echo heights for Kelvin (a,b) and MRG (c,d) convective (a,c) and stratiform (b,d) precipitation areas. Shadings represent fractional frequency, and the same shading scale is used in each plot. Altitude bins are centered on each 2 km layer of radar data (for example, the 1 km bin represents the 0-2 km altitude layer).

List of Tables

| | | |
|---|---|-----|
| 1 | The wave event-defining methodologies of this study and of the S06 study, along with the number of wave events and event-days defined using these methods. S06 also employed some smoothing parameters that are discussed in their study. | 103 |
| 2 | Calibration corrections applied to Kwajalein radar data for July-December 1999-2003 (from Houze et al. 2004). | 104 |
| 3 | Radar calibration corrections applied to the radar volumes of the trough events in this study (following Houze et al. 2004). Some periods of 2001 and all of 2002 and 2003 had no specified calibration correction (denoted here as N/A), so the radar volumes in these periods were not corrected. | 105 |
| 4 | Radar echo areas (km ²) using the long-range radar scans (radius=240 km, domain area \cong 180 248 km ² , 10-12 min frequency) corresponding to quartiles computed from distributions of cumulative area and cumulative frequency. ‘All’ refers to all July-December 1999-2003 scans. Kelvin and MRG areas are for the trough events in this study. Numbers in () show the [wavetype - all] difference. Long-range scans were unavailable for early July 1999 and most of October-December 2002, omitting 3 Kelvin events and 1 MRG event from these statistics. | 106 |

| | | |
|---|---|-----|
| 5 | <p>Statistics on the occurrences and characteristics of the three major horizontal precipitation organizations during our trough events – isolated, MCS, and convective line (see Section 3 for organization methodology). Frequencies of occurrence of organizational types were noted visually using convective-stratiform reflectivity maps, calculated from the 0-2 km altitude reflectivity layer of the three-dimensional volume scans (radius=157 km, domain area\cong76 752 km²), at 30 min intervals. Sizes and porosities were calculated using the objective blob detection algorithm (Section 4) on all Kelvin and MRG radar volumes.</p> | 107 |
| 6 | <p>Selected statistics of individual contiguous rain ‘blobs’ during our trough events using a 15 dBZ reflectivity threshold (Section 3). Orientation and aspect ratio statistics are only for blobs larger than 10 pixels. ‘Distance between’ is calculated as each blob’s closest neighbor in a given scan (measured between blob centroids). Many reflectivity standard deviation values were 0.01, so ‘modal standard dev.’ is only for standard deviation values above 0.01.</p> | 108 |
| 7 | <p>Total precipitation areas (km²), convective precipitation areas (km²), and stratiform precipitation areas in our trough dataset using to the three-dimensional radar volume scans (radius=157 km, domain area\cong76 752 km²) and corresponding to percentiles computed from distributions of cumulative frequency. .</p> | 109 |

TABLE 1. The wave event-defining methodologies of this study and of the S06 study, along with the number of wave events and event-days defined using these methods. S06 also employed some smoothing parameters that are discussed in their study.

| | Our Trough Events | S06 Wave Events |
|--------------------------------|---|--|
| Time Period | Jul-Dec 1999-2003 | Jul-Dec 1999-2001 Jul-Sep 2002 |
| OLR Filtering Spectral Windows | Wheeler and Kiladis (1999) Fig. 6 | Kelvin: Straub and Kiladis (2002) Fig. 1 MRG: Wheeler and Kiladis (1999) Fig. 3 |
| OLR Spatial Averaging Domain | 5-12.5 °N 162.5-170 °E | 0-15°N 165-170 °E |
| Wave Amplitude Requirements | Negative, $\geq 1.5\sigma$ for ≥ 24 h | Positive or negative, $\geq 2\sigma$ |
| Rain Area Requirements | None | $\geq 2\sigma$ |
| Number of Wave Events | 23 Kelvin 16 MRG | 22 Kelvin 22 MRG |
| Number of Wave Event Days | 25.5 Kelvin 16 MRG | 52 Kelvin 48 MRG |

TABLE 2. Calibration corrections applied to Kwajalein radar data for July-December 1999-2003 (from Houze et al. 2004).

| Time Period (YYYYMMDD) | Calibration Correction (dB) |
|---------------------------|--------------------------------|
| 19990701-19991231 | +6 |
| 20000701-20000821 | 0 |
| 20000822-20000925 | -3 |
| 20000926-20001022 | -1 |
| 20001023-20001120 | 0 |
| 20001121-20001212 | -3 |
| 20001213-20001231 | +1 |
| 20010701-20000806 | +1 |
| 20010807-20011202 | N/A (0) |
| 20011203-20011231 | +6 |
| 20020701-20021231 | N/A (0) |
| 20030701-20031231 | N/A (0) |

TABLE 3. Radar calibration corrections applied to the radar volumes of the trough events in this study (following Houze et al. 2004). Some periods of 2001 and all of 2002 and 2003 had no specified calibration correction (denoted here as N/A), so the radar volumes in these periods were not corrected.

| Calibration Correction | % radar volumes | | |
|------------------------|-----------------|-----|-------|
| | Kelvin | MRG | Total |
| -3 dB | 0 | 7% | 3% |
| 0 dB | 18% | 30% | 22% |
| +1 dB | 13% | 0 | 8% |
| +6 dB | 19% | 19% | 19% |
| N/A (0 dB) | 50% | 44% | 48% |

TABLE 4. Radar echo areas (km²) using the long-range radar scans (radius=240 km, domain area \cong 180 248 km², 10-12 min frequency) corresponding to quartiles computed from distributions of cumulative area and cumulative frequency. ‘All’ refers to all July-December 1999-2003 scans. Kelvin and MRG areas are for the trough events in this study. Numbers in () show the [wavetype - all] difference. Long-range scans were unavailable for early July 1999 and most of October-December 2002, omitting 3 Kelvin events and 1 MRG event from these statistics.

| Cumulative Area | | | | |
|----------------------|-------------------|-------------------|---------------------|----------------------------------|
| | 0.25 | 0.5 | 0.75 | Maximum Achieved Total Echo Area |
| All | 17 072 | 31 120 | 49 728 | 128 048 |
| Kelvin | 23 936 (+6864) | 37 392 (+6272) | 56 192 (+6464) | 90 752 |
| MRG | 21 008 (+3936) | 32 288 (+1168) | 45 600 (-4128) | 64 496 |
| Cumulative Frequency | | | | |
| | 0.25 | 0.5 | 0.75 | Total No. Samples |
| All | 3759 | 10 191 | 23 279 | 88 241 |
| Kelvin | 6831 (+3073) | 17 023 (+6833) | 33 855 (+10 576) | 2934 |
| MRG | 8207 (+4448) | 18 463 (+8272) | 31 503 (+8224) | 1 692 |

TABLE 5. Statistics on the occurrences and characteristics of the three major horizontal precipitation organizations during our trough events – isolated, MCS, and convective line (see Section 3 for organization methodology). Frequencies of occurrence of organizational types were noted visually using convective-stratiform reflectivity maps, calculated from the 0-2 km altitude reflectivity layer of the three-dimensional volume scans (radius=157 km, domain area \cong 76 752 km²), at 30 min intervals. Sizes and porosities were calculated using the objective blob detection algorithm (Section 4) on all Kelvin and MRG radar volumes.

| Organizational Statistics | | Kelvin | MRG |
|---------------------------|---|-----------------------------------|----------------------------------|
| Isolated Cells | % radar volumes with isolated activity | 92% | 91% |
| | % radar volumes with only isolated activity | 54% | 49% |
| | Typical cell size | 32 km ² | 32 km ² |
| MCSs | % radar volumes containing MCSs | 18% | 19% |
| | # wave events containing MCSs | 18 of 23 | 14 of 16 |
| | Median / Max MCS size | 10 814 / 58 897 km ² | 7 072 / 39 426 km ² |
| | % MCSs with porosity > 0.05 / > 500 km ² | 18 / 35% | 12 / 15% |
| Convective Lines | % radar volumes with convective lines | 9% | 3% |
| | # wave events with lines | 17 of 23 | 4 of 16 |
| | Line Orientation | 13 N-S, 5 NE-SW 1 E-W, 5 SE-NW | 0 N-S, 1 NE-SW 0 E-W, 5 SE-NW |

TABLE 6. Selected statistics of individual contiguous rain ‘blobs’ during our trough events using a 15 dBZ reflectivity threshold (Section 3). Orientation and aspect ratio statistics are only for blobs larger than 10 pixels. ‘Distance between’ is calculated as each blob’s closest neighbor in a given scan (measured between blob centroids). Many reflectivity standard deviation values were 0.01, so ‘modal standard dev.’ is only for standard deviation values above 0.01.

| Blob Statistic | | Kelvin | MRG |
|-------------------------------------|------------------------------------|------------------------|------------------------|
| Number per Scan | Freq. Dist. | Pos. Skew. Gaussian | Pos. Skew. Gaussian |
| | Mode | 28 | 37 |
| | Max | 87 | 114 |
| Distance Between | Freq. Dist. | Logarithmic | Logarithmic |
| | Mode | 12 km | 12 km |
| Orientation Clockwise from North | Freq. Dist. | Nearly Uniform | Nearly Uniform |
| Minor:Major Axis Aspect Ratio | Freq. Dist. | Gaussian | Gaussian |
| | Mode | 0.61 | 0.58 |
| Reflectivity | Freq. Dist. of Modal Blob Value | Logarithmic | Logarithmic |
| | Modal Blob Value | 16 dBZ | 16 dBZ |
| | Max Observed | 58 dBZ | 62 dBZ |
| | Modal Blob Standard Dev. | 4 dBZ | 4 dBZ |
| | Max Observed Standard Dev. | 21 dBZ | 22 dBZ |

TABLE 7. Total precipitation areas (km²), convective precipitation areas (km²), and stratiform precipitation areas in our trough dataset using to the three-dimensional radar volume scans (radius=157 km, domain area \cong 76 752 km²) and corresponding to percentiles computed from distributions of cumulative frequency.

| Cumulative Frequency | | | | | | |
|----------------------------------|--------|------|------|--------|--------|------------------------------|
| | | 25% | 50% | 75% | 90% | Ensemble Accumulated Area |
| Total Precipitation Area | Kelvin | 2347 | 5467 | 14 235 | 28 147 | 37 904 400 |
| | MRG | 3191 | 6967 | 14 613 | 21 635 | 20 150 240 |
| Convective Precipitation Area | Kelvin | 467 | 1371 | 3595 | 5455 | 8 407 944 |
| | MRG | 643 | 1687 | 3215 | 5187 | 4 612 220 |
| Stratiform Precipitation Area | Kelvin | 1527 | 3609 | 10 745 | 23 376 | 29 496 456 |
| | MRG | 2000 | 4957 | 11 465 | 18 488 | 15 538 020 |